Icarus 302 (2018) 514–536

Contents lists available at ScienceDirect

Icarus

journal homepage: www.elsevier.com/locate/icarus

The cascade from local to global dust storms on Mars: Temporal and spatial thresholds on thermal and dynamical feedback

Anthony D. Toigo[a,*], Mark I. Richardson[b], Huiqun Wang[c], Scott D. Guzewich[d], Claire E. Newman[b]

[a] Johns Hopkins University Applied Physics Laboratory, Laurel, MD, United States
[b] Aeolis Research, Pasadena, CA, United States
[c] Harvard-Smithsonian Center for Astrophysics, Cambridge, MA, United States
[d] NASA Goddard Space Flight Center, Greenbelt, MD, United States

ARTICLE INFO

Article history:
Received 1 June 2017
Revised 13 November 2017
Accepted 27 November 2017
Available online 5 December 2017

Keywords:
Mars
Atmosphere
Atmospheres
Dynamics
Meteorology

ABSTRACT

We use the MarsWRF general circulation model to examine the temporal and spatial response of the atmosphere to idealized local and regional dust storm radiative heating. The ability of storms to modify the atmosphere away from the location of dust heating is a likely prerequisite for dynamical feedbacks that aid the growth of storms beyond the local scale, while the ability of storms to modify the atmosphere after the cessation of dust radiative heating is potentially important in preconditioning the atmosphere prior to large scale storms. Experiments were conducted over a range of static, prescribed storm sizes, durations, optical depth strengths, locations, and vertical extents of dust heating. Our results show that for typical sizes (order 10^5 km^2) and durations (1–10 sols) of local dust storms, modification of the atmosphere is less than the typical variability of the unperturbed (storm-free) state. Even if imposed on regional storm length scales (order 10^6 km^2), a 1-sol duration storm similarly does not significantly modify the background atmosphere. Only when imposed for 10 sols does a regional dust storm create a significant impact on the background atmosphere, allowing for the possibility of self-induced dynamical storm growth. These results suggest a prototype for how the subjective observational categorization of storms may be related to objective dynamical growth feedbacks that only become available to storms after they achieve a threshold size and duration, or if they grow into an atmosphere preconditioned by a prior large and sustained storm.

1. Introduction

Dust storms on Mars are observed to exhibit a wide range of sizes, durations, and optical thicknesses (Briggs et al., 1979; Martin and Richardson, 1993; Martin and Zurek, 1993; Cantor et al., 2001; Wang and Richardson, 2015; Guzewich et al., 2015, 2017; Kass et al., 2016; Kulowski et al., 2017). Colloquially these storms have been grouped based primarily on their size, with references to "local", "regional", and "planet-encircling" (or "global" or "great") being common (e.g., Martin and Zurek, 1993). Based upon the extensive and nearly continuous dataset available from Mars Global Surveyor (MGS) through to Mars Reconnaissance Orbiter (MRO), other additional categorizations have been suggested based on both the spatial and temporal extent of the storm (Cantor et al., 2001), the seasonal date of large regional and global storm onset (Kass et al., 2016), or the location and mechanism of regional storm evolution (Wang and Richardson, 2015). Local dust storms are the most common occurring storm and their characteristics and spatial and temporal distribution have been examined in some detail (Cantor et al., 2001; Guzewich et al., 2015, 2017; Kulowski et al., 2017).

An important question prompted by the creation of these subjective categories is: to what extent do storms actually cluster into different "types" of storms and what physical mechanisms might exist that cause such clustering? For example, are the local and regional storms shown in Fig. 1 merely self-similar structures of different sizes or are there distinct dynamics that control these structures such that they are truly separate classes of storm? To illustrate this dichotomy, it might be argued that on the one hand the spectrum of storm sizes is a continuum and that the grouping of storms into labeled categories is an arbitrary, subjective, and "fuzzy" discretization of a natural, continuous distribution. A corollary of this argument would be that there are no threshold size- or

* Corresponding author.
E-mail address: Anthony.Toigo@jhuapl.edu (A.D. Toigo).

https://doi.org/10.1016/j.icarus.2017.11.032
0019-1035/

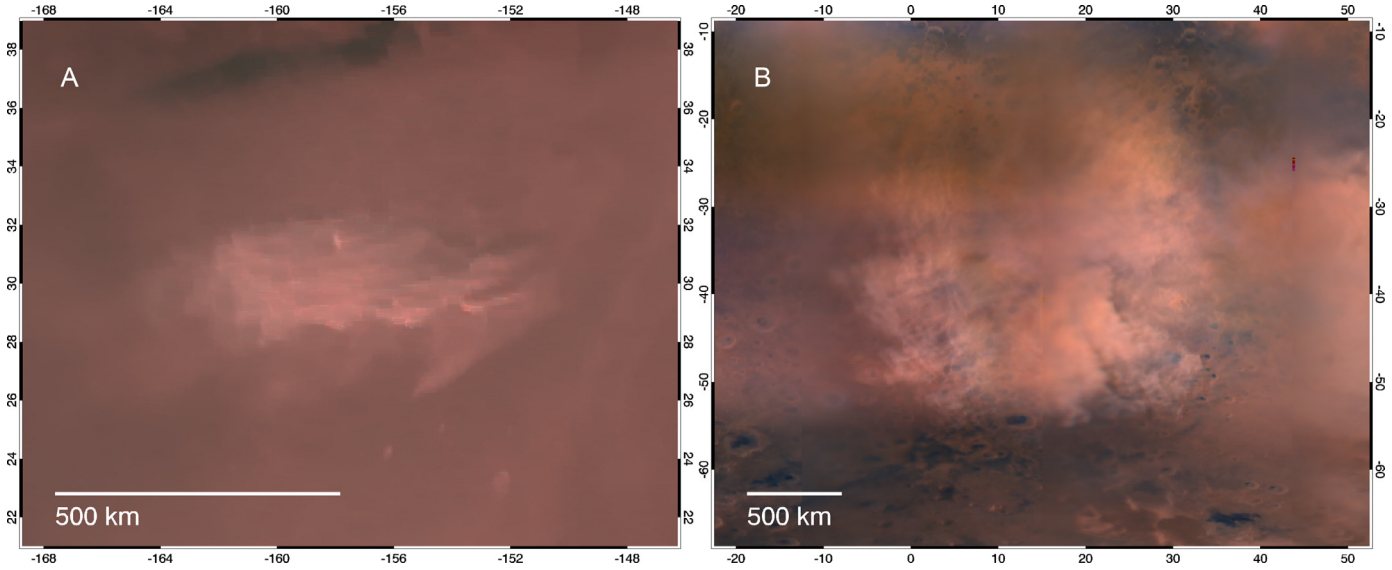

Fig. 1. Examples of (A) local and (B) regional dust storms seen in the Mars Daily Global Maps (MDGMs) assembled from Mars Reconnaissance Orbiter (MRO) Mars Color Imager (MARCI) camera images. (A) Local storm near Amazonis Planitia in MDGM B10_day27, Ls=291.9°. (B) Regional storm over Noachis Terra, west of Hellas, in MDGM B11_day27, Ls=309.7°. Boxes around each image show latitude and longitude intervals, while scale bars at the lower left of each image show the difference in relative size between the two storms. The scale bars are shown as a 500 km reference distance corresponding to the central latitude of each image. Note that both images use a simple cylindrical map projection and hence the 500 km scale bar changes in projected length at different latitudes; in particular, in case (B) the latitudinal variation of over 60° in the image means that the 500 km scale bar will change by approximately a factor of 3 between the top and the bottom of the image.

time-dependent feedbacks for storm development. Instead, there would be a dependence on stochastic parameters (e.g., background winds, supply of dust, etc.), and that, at an extreme, there would be only a very weak positive feedback on dust lifting, otherwise all storms would eventually grow to the largest extent. On the other hand, the contrary argument would be that the storm categories truly reflect deeper and objective divisions in the actual dust storm population. The corollary in this case would be that real physical mechanisms within the atmosphere must provide threshold (size and duration) and/or location dependent "gates" that allow storms to change from one category to another and create the gaps (the transitional pathways) between the categories. In this latter case, dust storm growth would represent a true cascade as new modes of growth became available to storms depending upon their size, duration, history, and location.

Some evidence that objective categorical definition has merit, at least in the case of distinct global dust storms, is provided by numerical modeling of global dust storm onset (Haberle et al., 1982; Schneider, 1983; Wilson, 1997; Newman et al., 2002; Basu et al., 2004). These models show that the presence of sufficient dust in the atmosphere fundamentally reconfigures the general circulation, with a significant expansion and intensification of the overturning ("Hadley") circulation. Further support for objective categorical distinction of storms is provided by the frontal/tidal mechanism for the development of "flushing" storms (Wang et al., 2003), where a distinct morphological subcategory of regional storms has been linked to a specific regional and seasonal window (the northern mid-latitudes in northern autumn and winter), and to a specific transitional mechanism (the constructive interference of the thermal tide with baroclinic frontal storms).

A generalization of the question of storm categorization is whether thresholds exist such that as storms grow they gain access to additional and potentially faster mechanisms of growth that are not available to smaller storms. The activation of such extra mechanisms of growth would then provide the physical distinctions between different storm type categories. Most local dust storms, which widely occur near the cap edge, at surface thermophysical property boundaries, and in association with local topography, generally dissipate within a few sols (e.g., Cantor et al., 2001; Guzewich et al., 2015; 2017; Kulowski et al., 2017). This suggests that the intrinsic growth mechanisms that are available to small storms are relatively slow compared to changes in the externally imposed thermal and wind state. Indeed, it is not clear how much of local storm growth is due to intrinsic feedbacks (such as an expanding periphery of dust lifting) and how much is due to changes in the externally imposed wind field independent of the dust storm (e.g., the apparent lack of feedback in the storms examined by Heavens (2017)). Irrespective of how the smaller storms initially grow, the question addressed in this paper is whether the ability of a storm to influence the atmosphere at some distance from the area of dust heating, and/or at some time after cessation of dust heating, changes significantly for storms above some threshold size, duration, and/or dust opacity. Distal influence then opens the possibility of distal feedback mechanisms of storm growth (e.g., more rapid expansion of the existing lifting area, activation of new lifting centers, increased rates of dust advection, deeper vertical mixing of dust, etc.) that are not available to smaller storms and would create a dynamically meaningful distinction between large local and small regional storms. Similarly, a lasting modification of the atmosphere by one storm that aids the growth of a subsequent storm allows for the physical categorization of sequential activation storms, as observationally described by Wang and Richardson (2015) and that may have been important in the origin of the 2001 global storm (Strausberg et al., 2005).

In this paper, we examine the scale-dependent feedback between local and regional dust storms and the regional and global atmosphere. We limit the study to consideration of only the thermal and dynamical feedback on the atmosphere in order to limit the investigation to feedbacks associated with the distal dynamical response of the circulation to the storm. We do not treat advection of dust aerosols nor the activation of additional dust lifting centers beyond the area of the originally imposed storm. We use a general circulation model (GCM) to examine the thermal and dynamical response of the atmosphere to the imposition of static dust storms (simulated as regions of increased dust optical depth) of differing physical extent, duration, and total optical depth. The strength of

Table 1
List of experiments discussed in this work. For storm locations, refer to Table 2 and Fig. 2. Optical depths are referenced to a wavelength of 0.67 microns. *The simulation of the regional storm at location 1 used an optical depth of 200 rather than 250 for both durations.

	Storm properties		
Experiment	Optical depth, τ	Duration (sols)	Location
Reference	No storms (climatology)	–	–
Local, $O(10^5$ km$^2)$	1, 3, 10, 30, 100, 250	1.5, 10.5	1, 2, 3, 4, 5, 6
Regional, $O(10^6$ km$^2)$	1, 3, 10, 30, 100, 250*	1.5, 10.5	1, 2

response is assessed by examining the degree to which the imposed storms influence the atmosphere in their proximity and the period over which the imposed storms influence the atmosphere after removal of the optical depth perturbation.

In Section 2, we describe the setup of the GCM experiments using the Mars Weather Research and Forecasting (MarsWRF) model, and describe our choices for storm category size and duration. We then proceed to describe the results of imposing "local" and "regional" scale storms in the model in Sections 3 and 4, respectively. Finally, we provide a summary and discussion in Section 5.

2. Experimental setup

All experimental simulations described in this paper were performed using the MarsWRF GCM (Toigo et al., 2012), the Mars-specific instance of the generalized planetary atmospheric model, planetWRF (Richardson et al., 2007). The simulations were all run at 2° horizontal resolution, with 52 vertical layers stretching from the surface to approximately 120 km altitude. All other physics parameterizations and model parameters are as described in Toigo et al. (2012), with the exception of the radiation parameterization of Mischna et al. (2012) that is used here.

Experiments were conducted with the goal of determining the size of the spatial, temporal, and opacity perturbations necessary for the thermal and dynamical state of the atmosphere at some distance from the storm to be affected. In other words, we seek a quantitative gauge of how much of a perturbation is required before the atmosphere external to the storm "senses" the presence of a storm. There are a great many feedback mechanisms potentially associated with dust storms and the spread of their influence to other locations. In this initial study, we specifically only consider the dynamical response to imposed dust storm radiative forcing. In this case, the atmosphere can respond to the imposed forcing by a range of dynamical mechanisms, such as wave excitation and the development of thermally-direct circulations, that modify temperature and winds distal to the site of forcing. At the scale of regional-to-global storm transitions, it is these kinds of remote (or teleconnection) dynamical feedbacks that are thought to be of prime importance (e.g., Schneider, 1983) as they can operate much more quickly on long length scales than advective processes and also fundamentally reconfigure the nature of the circulation.

In order to examine the impact of local and regional storms upon the atmosphere, we developed a set of idealized storms with differing location, lateral extent, duration, total column optical depth, and vertical extent of dust optical depth perturbation. See Table 1 for a list of experiments and their major characteristics. The impact of the perturbations on the state of the atmosphere is quantified by comparison with a storm-free control simulation, with the method of comparison described in more detail in Sections 3 and 4. Dust optical depth is fully prescribed and does not respond to the model winds. The background atmospheric dust optical depth for the reference simulation follows the spatial and temporal function described by Montmessin et al. (2004). This reference run forms the initial state for all perturbation cases, and was previously spun-up for several years in order to equilibrate the seasonal CO_2 cycle (Guo et al., 2009). All dust storm simulations were conducted in early northern fall at a solar longitude of approximately Ls=220°, which lies within the broad span of the Martian "dust storm season" (roughly Ls=180°-330°) and is when a large number of storms are often observed (e.g., Guzewich et al., 2017). Given the nature of the results for local storms (described in Section 3), it seems unlikely that the limitation to one seasonal date will be of any consequence. For regional storms, we suspect that season would not have a strong impact on the core findings of this work regarding whether a threshold storm size is needed to produce a distal effect, but do not investigate this here.

Locations of storms imposed and investigated within this study are listed in Table 2 and shown in Fig. 2. All are sites of relatively frequent dust storm occurrence, as seen in dust storm occurrence frequency maps in Guzewich et al. (2017), with activity observed at or near Ls=220° during at least one of the Mars years in their survey. Despite the wide geographic range of chosen sites, results were quite similar at all locations, and thus only results from western Hellas (location 1) and Chryse Planitia (location 2) are shown or described in the following sections. Results for the other sites are, however, included in the supplementary materials.

For the two primary study locations, "regional dust storms" (larger than order 10^6 km^2) were imposed in additional sets of simulations beyond the "local storm" (of order 10^5 km^2) simulations and storm-free "reference" case. The size of the imposed dust storms was based on both the statistics of observed dust storms reported in Guzewich et al. (2017) and the definition of storm size categories described in Martin and Zurek (1993). The location and size of the regional storms for locations 1 and 2 are indicated by the larger boxes in Fig. 2. For all simulations and locations, the "local" storms were designed to be a region 3×3 gridpoints in size (corresponding to 6° longitude by 6° latitude at the resolution used in these simulations, and thus representing an area of approximately 10^5 km^2), while the "regional" storms were designed to be a region of 31×15 gridpoints (62° longitude by 30° latitude, with an area of approximately 5×10^6 km^2).

For each of the two storm size categories, two durations were examined. These durations were 1.5 sols (for short storms) and 10.5 sols (for long storms), where "sol" refers to one Martian solar day. The total duration of each experiment bracketing these storm perturbations was 10 and 20 sols, respectively. The first approximately 2.5 sols of each simulation was unperturbed from the spun-up reference simulation, and then at the next occurrence of roughly local noon at the imposed storm location, the dust optical depth was increased to reflect the occurrence of a storm. Thus, for the 1.5-sol duration storm experiments, after cessation of the storm there followed a further 6 sols of after-storm simulation, while for the 10.5-sol duration storm experiments, after cessation of the storm there followed a further 7 sols of after-storm simulation.

A duration of 1.5 sols was selected to represent, roughly, the minimum resolvable storm duration from Mars orbital observations, i.e., a storm seen on one sol but not on the prior or subsequent sol, and without knowledge of exactly when the storm started or ended. The choice of 1.5 sols also results from starting

Table 2
List of locations where dust storms were imposed in simulations. The approximate geographic region and central latitude and longitude of each location are listed. See also Fig. 2 for a map of the locations.

Imposed Dust Storm Locations			
Location	Region	Central Latitude	Central Longitude
1	Western edge of Hellas Planitia	37°S	55°E
2	Southeast of Tempe Terra near Chryse Planitia	33°N	63°W
3	Syria Planum	17°S	101°W
4	Acidalia Planitia	57°N	11°W
5	Terra Cimmeria	57°S	139°E
6	Arcadia Planitia	37°N	173°E

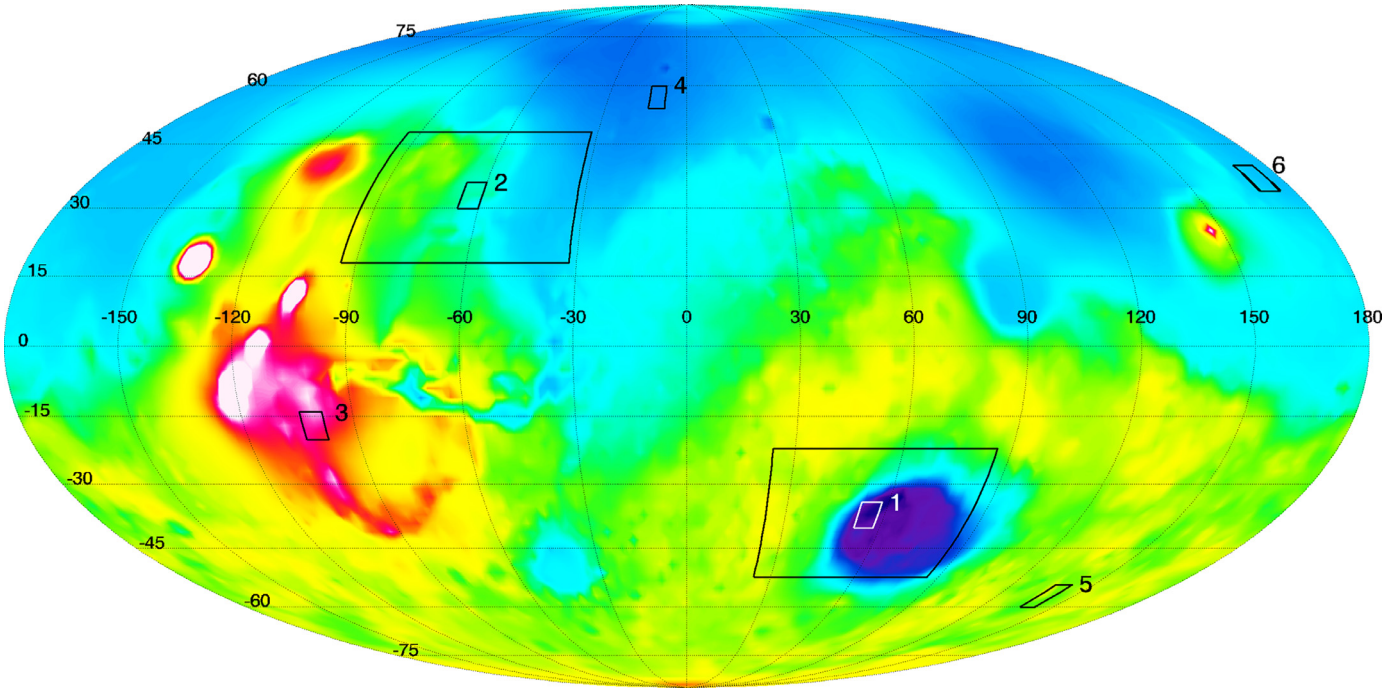

Fig. 2. Location and approximate size of simulated local dust storms (black or white boxes) in this work, shown on MOLA topography for reference. The larger boxes around locations 1 and 2 are the sizes and locations of the imposed regional dust storms in their respective simulations.

the imposed storm around noon local time (as a time of large turbulent activity), and allowing it to continue to exist for the remainder of that sol plus one further full sol. Our intent in this design was to apply the simulated storm forcing for at least one full diurnal cycle (with some extra margin of time) in order to capture the effect on the circulation at all local times during a sol and thus maximize the ability of these short duration storms to affect the atmosphere in their vicinity. The 10.5-sol duration storms were designed to sample the long-duration tail end of the observed storm duration distribution (Guzewich et al., 2017). This choice of the duration of short and long storms allows us to effectively bracket the vast majority of the observed range of storm durations, and to examine whether a threshold in duration exists somewhere between those two extremes.

The imposed storm simulations use the same background atmospheric dust vertical optical depth distributions as the reference case (Conrath, 1975; Montmessin et al., 2004), with the imposed storms added to this base state. Our choice of how far to extend these storms in the vertical is guided by: improved understanding of the vertical distribution of dust in different types of dust storms resulting from limb sounding data analysis (Heavens et al., 2015; Kass et al., 2016), the need to keep the experiments consistent (and thus remain intercomparable), and the need to keep the range of phase space explored to a reasonable size. For local storms, we make the default assumption that storm dust is limited to within the lowest 20 km of the atmosphere. The observations suggest that this confinement of dust likely provides the most accurate representation of local storm dust vertical mixing (Heavens, 2017). For larger storms, more complex structures involving near surface dust concentration maxima and upper level detrainment layers, superposed upon a background haze, appear more realistic, but with the depth and nature of the detrained layer variable between different storms (Heavens et al., 2011; 2015; Guzewich et al., 2013). In order to be able to directly compare our local and regional storms, and because of the open-endedness of prescription of possible detrainment layers (in height, thickness, optical depth, etc.), we decided to prescribe regional storm dust vertical distribution in the same way as for local storms. As such, our default imposed storm experiments prescribe storm-enhanced dust opacity extending from the surface to an elevation of 20 km above the surface. Above this sharp cloud top the vertical optical depth profile returns to a Conrath-like functional form (i.e., uniform mixing ratios for most of the height up to a cap altitude) but now based on the reference optical depth described by the climatological mean (e.g., Montmessin et al., 2004). Tables 1 and 2 summarize the range of simulations performed, listing storm sizes, durations, locations, and strengths/opacities. We additionally conducted experiments in which the dust opacity within the storm was perturbed throughout

the whole Conrath-like profile, while maintaining a capping altitude around 40 to 75 km depending on latitude (Montmessin et al., 2004). This did not change the qualitative results, however, and thus these results are not shown in this paper, although we briefly comment upon them in Section 5.

We define storm "strength" in terms of the imposed total dust optical depth, referenced to a wavelength of 0.67 microns (Colburn et al., 1989) and quoted for a 700 Pa reference level. For each imposed storm, the perturbation optical depth was held fixed throughout the entire duration of the storm. The dust optical depth (or equivalently, the underlying dust mixing ratio) was not allowed to advect or evolve. For each of the previously mentioned sets of storm parameters (location, size, and duration), 6 simulations were performed with optical depths ("τ") of 1, 3, 10, 30, 100, and 250 (or 200), although for clarity of plotting we do not show results for the τ=1 case (as it is in general very similar to the τ=3 case) nor for the τ=100 case (which is generally similar to the τ=250 case, albeit less intense).

The choice of the range of simulated dust storm optical depths was motivated by the desire to fully bracket with confidence the actual range of optical depths of local storms and lifting centers within regional storms. The first factor of ten of optical depth range (1–10) has conventionally been used as a representative benchmark in numerical simulations of global storms for decades (e.g., Haberle et al., 1982), and is supported at large horizontal length scales by orbiter thermal infrared observations (Martin and Richardson, 1993; Smith, 2008; Kleinböhl et al., 2009). The upper range of plausibility is less well determined from observations but what is not widely recognized is that upward-looking observations have not been undertaken within active lifting centers of local or regional storms. For example, the famous Viking Lander 1 storm of Sol 1742 (Moore, 1985) was not observed "in action" by the upward looking opacity sensor. In addition, orbiter remote sensing techniques generally saturate at optical depths much above 5–10. As such, it is very unlikely that the optical depths representative of active dust lifting have ever been accurately measured. Some gauge of plausible upper limits of real dust cloud optical depths can be taken from the fact that many local storms (and portions of regional storms) develop discrete sharp edges ("texture") and that they completely obscure the underlying ground (Guzewich et al., 2015; 2017; Kulowski et al., 2017). Indeed, terrestrial clouds that one might observe on a typical day generally have very steep gradients of optical depth to define the visible cloud edge. For the sharp edges of a typical terrestrial water cloud, the extinction coefficient, which is the optical depth per line-of-sight distance, is in the range of 0.005-0.1 m^{-1}. In the extreme case of visibly crisp cloud edges, this implies that an optical depth of 3 is obtained only 30 m into the cloud (Liou, 1992). A good empirical sense of what optical depth 3 hazes vs. optical depth $\geq$250 clouds look like can be gained by examining detailed multi-angle and multi-spectral orbiter images of terrestrial clouds such as those in Figs. 3 and 5 of Marchand et al. (2010). As such, to be certain of capturing the full plausible range of dust storm optical depths, we extend the logarithmic sampling of optical depth from the more commonly assumed (1–10) range to additionally include much more extreme values (up to 250).

3. Local storm results

3.1. Influence of dust optical depth and distribution on heating and temperature profiles

The net aerosol radiative heating and temperature vertical profiles for the prescribed short-period (1.5 sol) local storms at location 1 are shown in Fig. 3 for the unperturbed reference case and the τ=3, 10, 30, and 250 cases. As mentioned previously, only the cases in which imposed additional dust is placed within the lowest 20 km of the atmosphere are shown. The profiles are shown for the gridpoint at the center of the prescribed storm at 2 PM local solar time two sols prior to the storm (dashed), at 2 PM during the second sol of the storm (solid), and at 2 PM two sols after the storm imposition has ended (dotted).

The dominant feature of all of the imposed storm heating rate profiles is the sharp heating maximum at the cloud top at 20 km. This sharp peak is related to solar radiation that has passed rather freely (i.e., with relatively little scattering or absorption) down through the upper reaches of the atmosphere and has only encountered significant absorption optical depths at the cloud top. The heating profiles show two main trends with increasing optical depth: a substantial increase in the net aerosol radiative heating as the optical depth is increased, and also a sharpening of the peak of the radiative heating with optical depth. This sharpening just below the dust cloud top corresponds to the rapid increase in absorption with depth near the dust cloud top when the optical depth is larger. The gradient in absorption can also be expressed as a gradient in transmission, which contributes to the calculation of the familiar weighting functions used in remote sensing, and thus these dust heating profiles in some sense depict a peaked weighting function. Above the peak of this weighting function, few dust particles are available to absorb the incoming sunlight, while below the peak little insolation remains (at wavelengths in the dust absorption bands) to be absorbed by the dust. The weighting function is highly peaked in these storm cases, since the atmosphere is relatively clear all the way down to the lower atmosphere, at which point the suddenly greater density of particles inside the storm cloud yields a much sharper opacity contrast (a greater extinction coefficient), hence much greater absorption per unit vertical distance, and consequently creates what would appear to an orbital observer to be a distinct textured dust cloud top. As the column optical depth increases, this effect is intensified, leading to an increasingly distinct cloud top.

The maximum heating rates are very large. They correspond in many cases to significant perturbation of the thermal profile, but it should also be noted that these values do not occur over the full diurnal cycle, that much heat is diffused laterally away from the columns heated by the storm, and that energy is vertically mixed and transported away from the cloud top. The high levels of cloud top heating are conceptually consistent with the idea of high levels of buoyancy generation (e.g., Spiga et al., 2013), though we do not examine in this paper the mesoscale dynamics of the storm response to this heating or any resultant deep vertical mixing (other than the vertical thermal mixing generated by the model planetary boundary layer mixing parameterization). As an aside, we note that the vertical wavelength of the heating structure (approximately 30 km) is comparable to that of the diurnal tide, and while the lateral extent of the storm is very small, energy could possibly be pumped into the diurnal tide if these storms were sustained for many sols.

Irrespective of the total optical depth, the post-storm atmosphere (dotted lines) appears very little perturbed from its pre-storm state (dashed lines) in all cases, foreshadowing the major results from the analysis of short duration local storms that will be described in the following subsection.

3.2. Local, short duration (1.5 sol) storms

Local storms were initiated in one of six locations (as listed in Table 2 and illustrated in Fig. 2) for a period of 1.5 sols for each of the four storm strengths cases listed in Table 1. The modeled atmospheric response to these imposed storms was examined by calculating the difference (deviation) of relevant atmospheric fields (temperature, winds, and surface wind stress) from the val-

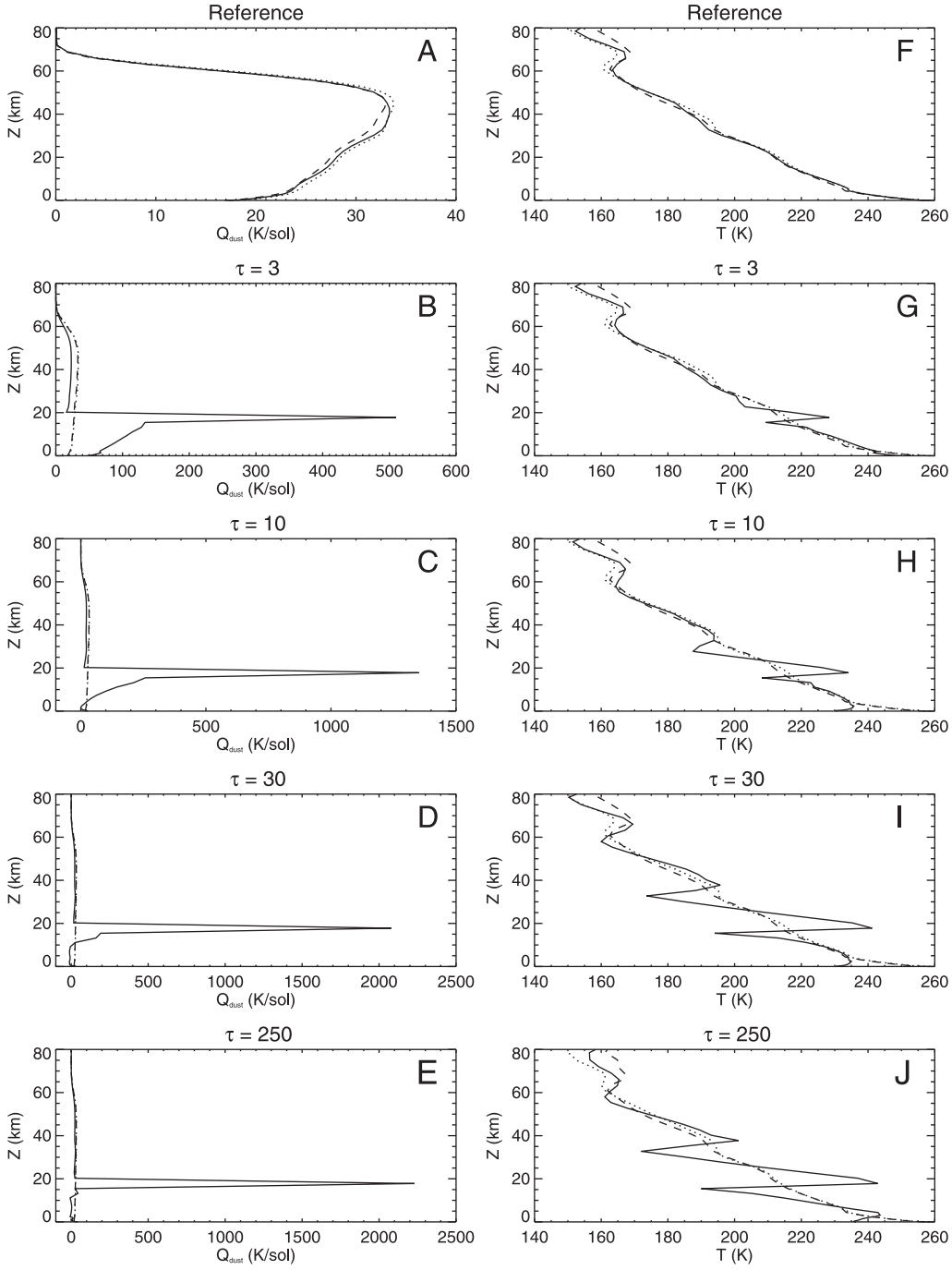

Fig. 3. Vertical profiles of dust aerosol heating rate (A–E) and temperature (F–J) for the location 1 local short-period (1.5 sol) dust storm simulations, each varying the optical depth of the storm (shown on each panel title; see Table 1 and main text for details). In each panel, three profiles, each at approximately 2 PM local time, are shown: 2 sols before the storm is initiated (dashed), during the storm (solid), and 2 sols after the storm has stopped (dotted).

ues generated by the model in the reference (no-storm) simulation at the same locations and times. To assess changes within the storm area, the values at the gridpoint at the center of the imposed storm were examined. The central gridpoint was chosen to sample the location of maximum storm response. To assess changes exterior to the storm, we examined the values within a halo two gridpoints away from the storm edge. Fig. 4 provides a pictorial representation of the numerical model grid box area of the imposed local storm and of the halo of exterior analysis gridpoints used. We show the locations of the temperature gridpoints; in MarsWRF, wind gridpoints are offset slightly from temperature gridpoints (see Richardson et al. (2007)), however winds are interpolated to the temperature gridpoints before being plotted in all Figures shown in this paper.

The two major issues we are interested in examining are (1) whether local storms generate consequential changes to the environment exterior to the storm while the storm heating exists, which might suggest a mechanism for the storm to spread beyond the heated area via induced dynamics, as well as (2) whether changes are generated after the storm perturbation has ceased, which might suggest a mechanism for extending the storm in time or for one local storm to pre-condition the atmosphere for a subsequent event. We briefly describe the differences between the simulations, and then comment on whether we believe these differ-

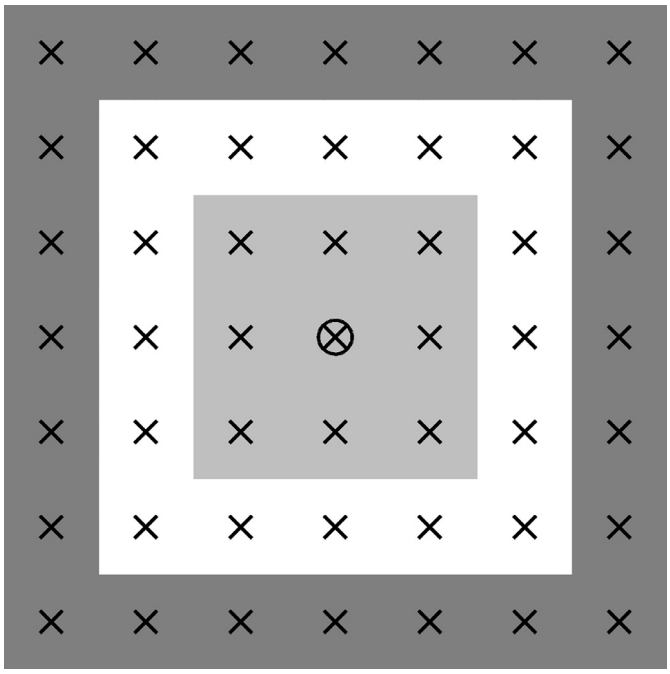

Fig. 4. Schematic showing how statistics were calculated for analysis of the local storms simulations. The "X" symbols represent numerical model gridpoints. The circled X is the gridpoint at the center of the prescribed storm. The light gray area is the area of the simulated local dust storm, in all cases, 3 gridpoints in both latitudinal and longitudinal extent. The dark gray area is the "halo" of gridpoints that are outside of the dust storm, but still close enough to be approximately representative of the same regional meteorology.

ences to be of consequence. Only location 1 results are described here, as the other regions show the same general behavior (see figures in the supplemental material).

Fig. 5 shows maps of the modeled horizontal winds and air temperatures during the storm at a local time of 2 PM and their deviations from the non-storm reference simulation, for the short local dust storm imposed at location 1. The leftmost column of panels shows the air temperature near the surface (at an altitude of roughly 20 m) as a color scale field with wind vectors at this level superposed, while the third column from the left shows the same information but for an altitude of roughly 30 km. The second and fourth columns show the deviation of the air temperature and horizontal wind from the non-storm reference case for both altitudes, respectively. From top to bottom, the simulations shown are the unperturbed reference, τ=3, 10, 30 and 250 cases (see Table 1).

The maps show relatively little influence of the storm upon any variable, except for near-surface air temperature, until the optical depth reaches τ=10. In all storm cases, the 20 m air temperature is reduced by the storm. This cooling results from the shading of the lower atmosphere and surface by the dust. At the surface, this cooling results in generally divergent flow at the storm edge, but with exceedingly small perturbation values in all cases. The layer at 30 km sits near the thermal minimum above the dust cloud top. At an optical depth of τ=10 and above, the influence of the vertical wave structure seen in Fig. 3 is thus very pronounced.

The lingering impact of the imposed storms two sols after the imposed dust storm was removed is illustrated in Fig. 6, which uses the same format as Fig. 5. Fig. 6 rather clearly shows that the atmosphere is effectively unperturbed after 2 sols regardless of whether the imposed storm had an optical depth of 3, 10, 30, or 250. Even for the τ=250 storm, the air temperatures at upper levels are only perturbed by a few K, primarily as a relative cooling of the atmosphere to the south of the storm. The wind is perturbed by a few m/s relative to the reference case, with some mild divergence from the relative cooled region and with some mild convergence toward the small, relatively warmed region.

The influence of the imposed storms on the atmosphere is better quantified in Figs. 7, 8, and 9, which show model output for every 2 hours (where we use "hour" to represent 1/24th of a Martian sol) over the entire span of the experimental simulation. These plots show the variation in a given atmospheric quantity between the reference and storm cases (as square symbols), and allow it to be compared to the typical variation (as given by the standard deviation over the region of interest) of the same atmospheric quantity within the reference case. In this way, the significance of the variation between a given storm case and the reference case can be assessed. Where the variation between the reference and the storm case is smaller or comparable to the natural variability of the reference case, we have a quantitative means of determining that the storm influence is not significant. Conversely, if the variation between the storm case and the reference case is much larger than the natural variability within the reference case, we may confidently state that the dust storm impact on the atmosphere is significant.

Fig. 7 confirms quantitatively what we concluded from examination of the temperature and wind field maps. It shows that the near surface (20 m) and upper (30 km) levels of the atmosphere are not significantly perturbed, either interior or exterior to the storm, after the dust optical depth perturbation is removed. During the storm, the atmosphere within the storm is significantly perturbed for $\tau \geq 10$ at the 30 km level and for all optical depth cases for the near surface atmosphere. Near the surface, temperature variations can be tens of K during and interior to the storm. Comparison with Fig. 5 shows this is generally due to strong shading and cooling of the surface and near-surface atmosphere, with the largest variances from the non-storm reference case occurring during the daytime, but also with significant, albeit smaller, heating perturbations associated with increased infrared cooling to space during the night.

The dynamical impact is better assessed by examining the wind field and associated surface wind stresses (Figs. 8 and 9). The information in these plots is presented in a similar format to that for air temperature shown in Fig. 7. The plots show that winds exterior to the storm are never significantly different than would be expected based on natural variability within the reference simulation. Interior to the storm, low altitude wind speeds are shown to only significantly exceed normal variability during the daytime, and even then by only 1 or 2 m/s. This is consistent with the near-surface air temperature predictions, and with the fact that the largest impact of the short-duration local storms involves shading of the daytime surface from solar insolation. At upper altitudes (30 km), the wind speed deviation is somewhat higher, reaching as much as 10 m/s for the larger dust opacities. Interestingly, the upper level winds for the largest optical depth case are perturbed long after the cessation of the imposed dust storm heating. This is due to the relatively long time required for the large approximately 30 km wavelength vertical wave structure set up by the imposed storm in this simulation to be damped out by the atmosphere.

Surface wind stress variance relative to the non-storm reference case is shown in Fig. 9. These plots show that exterior to the storm, wind stresses are not significantly perturbed relative to natural variability even during the storm, irrespective of optical depth. Interior to the storm, by contrast, the stress variation is briefly increased above natural variability for some storm cases during the period of storm imposition. The variances have maximum positive deviations of up to 10^{-2} Pa, of the correct order of magnitude to potentially initiate saltation and saltation-based wind stress dust lifting (e.g., Newman et al., 2002; Basu et al., 2004; Ayoub et al., 2014). Even interior to the storm, however, wind stresses drop be-

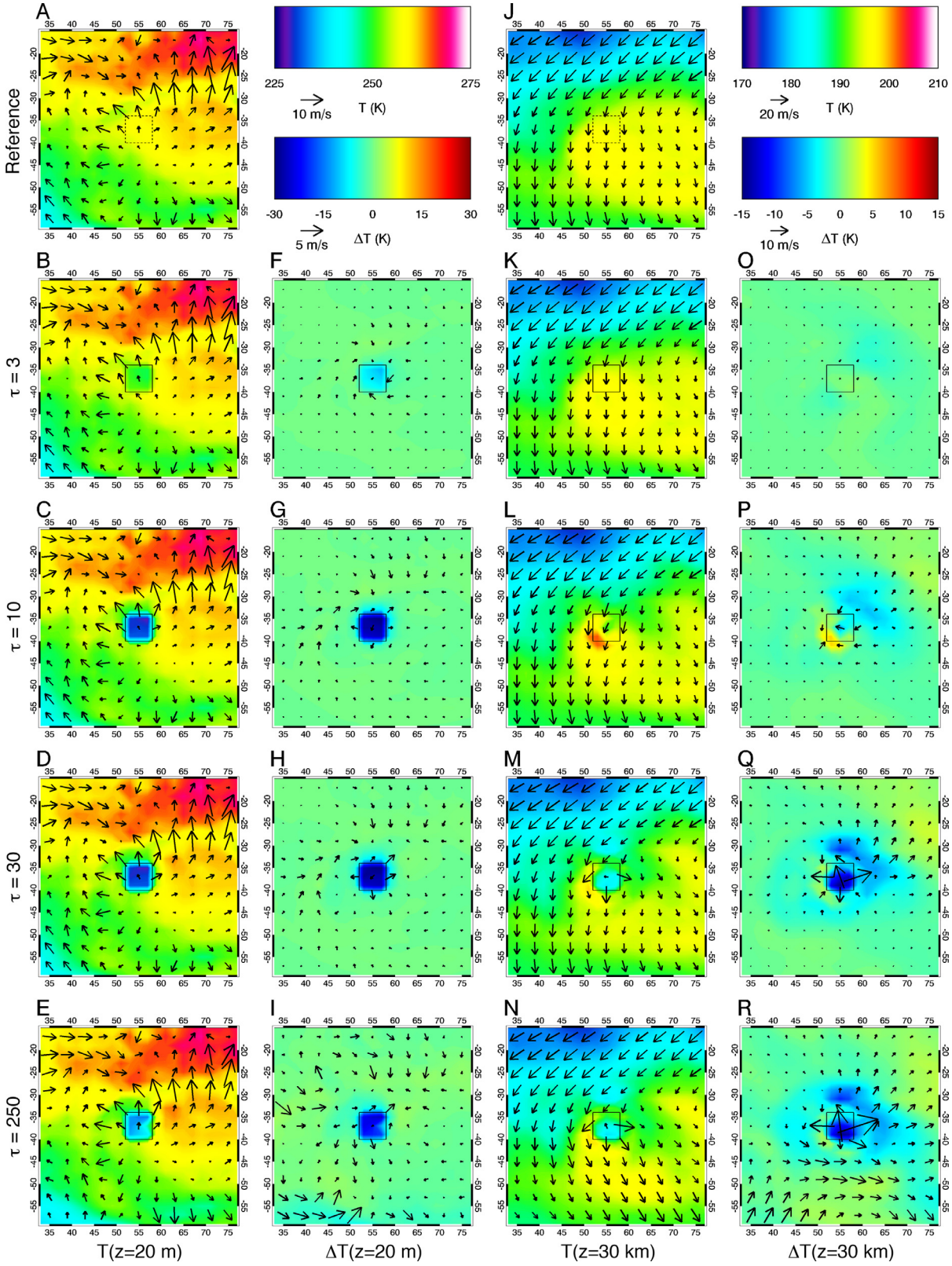

Fig. 5. Maps of near-surface (A–E, far left column, approximately 20 m altitude) and mid-atmosphere (J–N, third column from left, approximately 30 km altitude) air temperatures (colors) and horizontal winds (arrows), and differences (F–I, second column from left, near-surface; O–R, far right column, mid-atmosphere) of those temperatures and horizontal winds from the reference (storm-free) simulation in the location 1 1.5-sol local storm simulations. Local time shown is approximately 2 PM at the storm center during the complete sol of storm activity, i.e., the fourth sol of the overall simulation. (A,J) reference (storm-free) simulation; (B,F,K,O) τ=3 simulation; (C,G,L,P) τ=10 simulation; (D,H,M,Q) τ=30 simulation; (E,I,N,R) τ=250 simulation (optical depths for each row are also shown at the left edge of each row). Square black boxes overlain in the center of each map show the areal extent of the imposed local storm. At the top of the second (near-surface atmosphere) and fourth (mid-atmosphere) columns, color scales for air temperature (upper) and air temperature difference (lower) maps are shown, with arrow scales for the horizontal wind (upper) and horizontal wind difference (lower) shown just below them. Note that wind vectors are only shown for every other gridpoint in each direction.

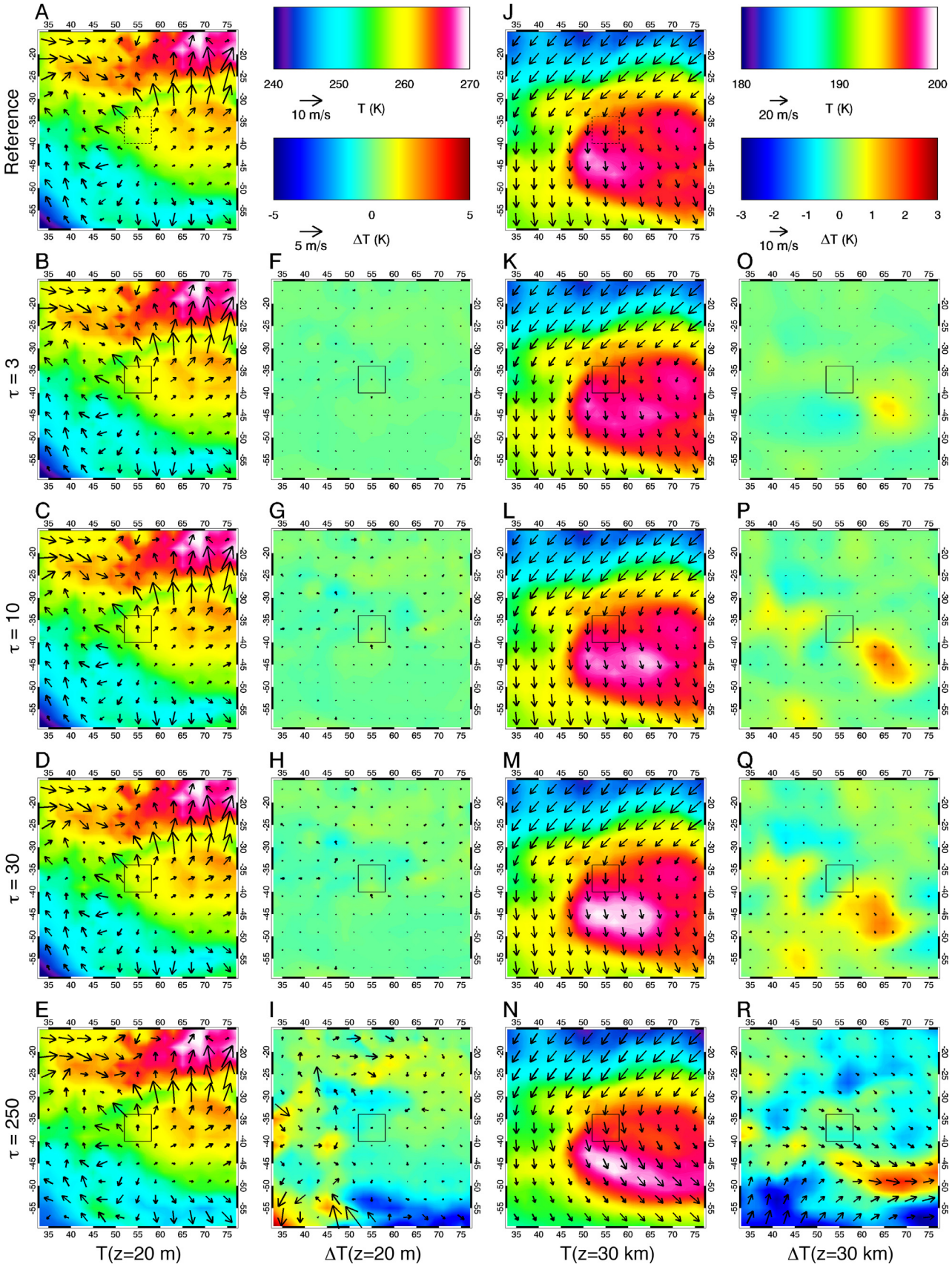

Fig. 6. Same as Fig. 5, except the time shown is approximately 2 PM local time at the center of the storm 2 sols after the storm has stopped. Note the change in color scales.

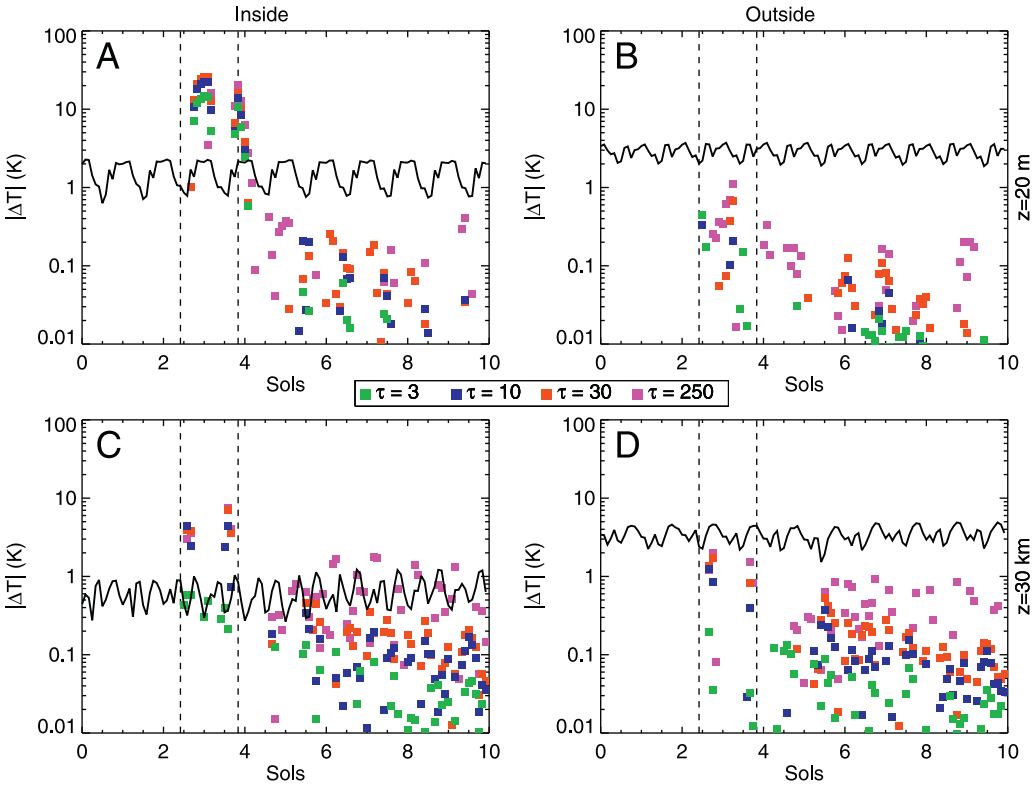

Fig. 7. Temperature absolute value differences (colored squares) in location 1 1.5-sol local storm simulations relative to the storm-free case during the course of the simulations. The top row (A–B) shows near-surface (approximately 20 m altitude) air temperature differences, while the bottom row (C–D) shows mid-atmosphere (approximately 30 km altitude) temperature differences. For the left column (A,C), the panels show the difference of the central gridpoint of the 9 gridpoint area of the simulated storm area (light gray area and circled X in Fig. 4). For the right column (B,D), the differences are calculated with respect to the average of the halo of gridpoints exterior to the prescribed storm (the dark grey region in Fig. 4). In each panel, the vertical dashed line shows the starting and ending times of the prescribed storms, while the solid line shows the standard deviation of temperatures in the reference simulation over the region of interest, i.e., over the 9 gridpoints of the simulated storm area in (A) and (C), and over the exterior halo of gridpoints in (B) and (D). In all panels, the color of the square indicates the optical depth of the storm in the simulation (see key in center of figure). Also note the logarithmic scale on the vertical axis.

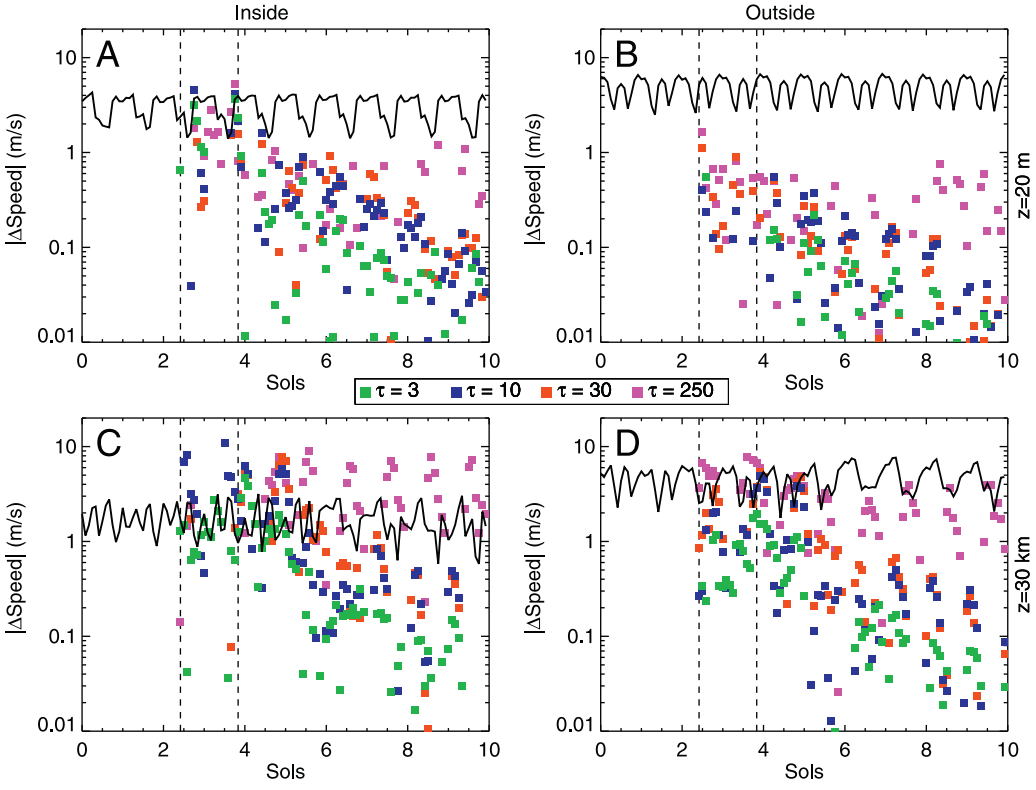

Fig. 8. Same as Fig. 7, except showing absolute value differences and standard deviations of horizontal wind speeds.

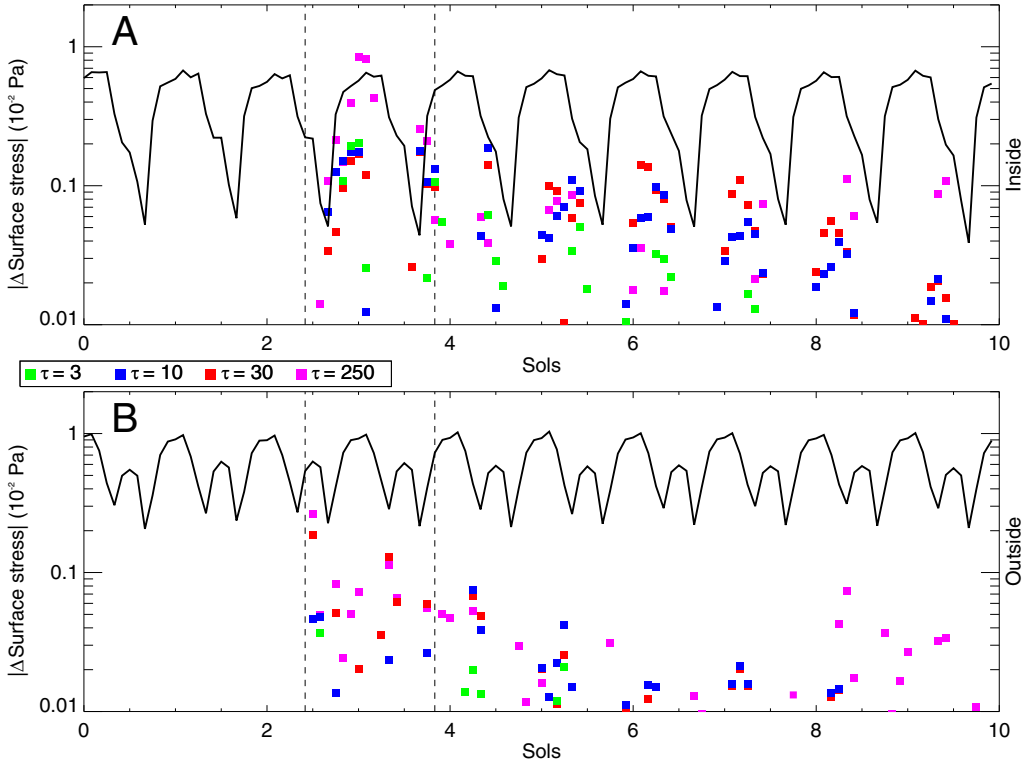

Fig. 9. The absolute value difference of surface wind stress (colored squares) in location 1 1.5-sol local storm simulations relative to the storm-free case during the course of the simulations. (A) The difference of the central gridpoint of the 9 gridpoint area of the simulated storm area (light gray area and circled X in Fig. 4). (B) The difference of the average of the halo of gridpoints exterior to the prescribed storm (the dark grey region in Fig. 4). In each panel, the vertical dashed line shows the starting and ending times of the prescribed storms, while the solid line shows the standard deviation over the region of interest, i.e., over the 9 gridpoints of the simulated storm are in (A), and over the exterior halo of gridpoints in (B). In all panels, the color of the square indicates the optical depth of the storm in the simulation (see key in left middle).

low natural background variability as soon as the imposed storm optical depth is terminated.

In this section, we have only described in detail the results for location 1. The other locations confirm the general behavior that short period local storms do not significantly modify the surface wind fields or stresses exterior to the storm location, or in the region of the storm after the cessation of imposed dust optical depth forcing (see supplemental figures).

3.3. Local, long duration (10.5 sol) storms

The 1.5 sol storms described in Section 3.2 correspond to the preponderance of local storm durations as observed from Mars orbiter cameras. However, it is interesting to consider whether more sustained application of the same storm forcing, i.e., through continuous imposition of an increased dust optical depth, would generate a larger exterior or interior response. In other words, is there a gradual "build up" in the atmospheric response to a local storm if it is imposed on a timescale much longer than the Martian atmospheric radiative time constant, which is of order 1 sol near the surface (Goody and Belton, 1967)?

The surface wind stress deviation results for the imposition of a local storm at location 1, but imposed for a period of 10.5 sols, are shown in Fig. 10 and can be directly compared with Fig. 9. Indeed, Fig. 10 shows that the daily response interior and exterior to the storm, and during and after the storm, are essentially the same regardless of whether the storm is imposed for 1.5 or 10.5 sols. For storms of both duration, there is a hint of a residual effect for the sol after the storm ends, but in either storm, the effect is still smaller than the background variability. In short, no residual or cumulative effect of the imposition of a local storm is apparent as a result of sustained dust loading. This result is general to all six locations examined in this study (not shown).

These results suggest that local dust storms of this size, even those with very high opacities, may not be able to grow purely via thermal perturbations that produce increased local surface wind stresses and hence dust lifting. Note that the observation that some fraction of local storms on Mars grow to larger scales tells us nothing about whether these storms grow through internal feedback dynamics (i.e., increased dust lifting triggered by thermal perturbations of the storm) or through externally imposed conditions (i.e., existing atmospheric flows not associated with the storm, such as baroclinic fronts). Our results also suggest that simple feedback of dust optical depth on local lifting may not be sufficient by itself to force local storm growth in the absence of lateral advection: the simulations cover the full range of plausible dust optical depths, such that irrespective of how much dust is present in the column, lateral storm expansion (by increasing wind stresses above the lifting threshold in areas exterior to the imposed storm) would not be accomplished. Our simulations are intrinsically synoptic in scale, and do not include interactive dust, and thus we cannot rule out the importance of linkages between dust lifting, dust transport, and mesoscale dynamics, but note that if these processes are important, they are also neglected in all interactive global dust cycle modeling studies to date. More fundamentally, by being able to isolate the dynamical response to the imposition of the static thermal signature of dust storms, the simulations in this paper provide a clear connection between cause and effect and provide a baseline against which fully interactive dust simulations can be compared in order to assess impacts uniquely ascribable to dynamical dust feedbacks.

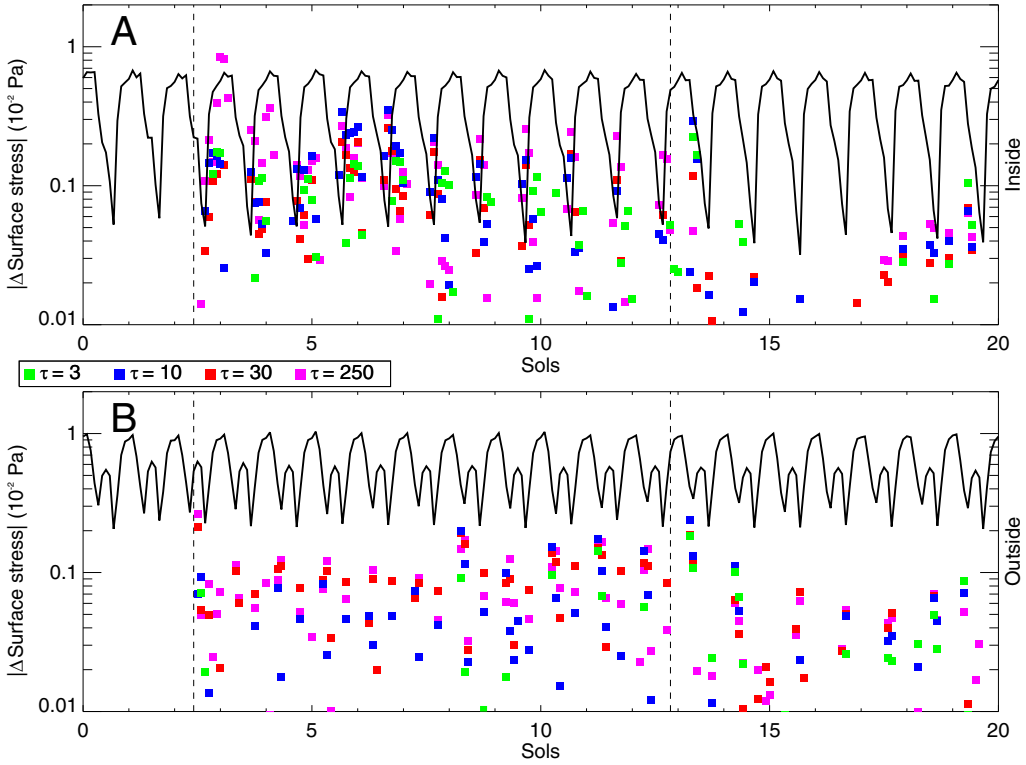

Fig. 10. Same as Fig. 9, except for location 1 10.5-sol local storm simulations.

4. Regional storm results

The idealized local storms described in Section 3 were unable to significantly perturb the atmosphere other than directly within the area of dust opacity augmentation and only while the increased optical depths were imposed. This result was independent of the period of imposition of the storm opacity, for reasonable durations of local storms (i.e., spanning the range of durations measured from observations). Based on prior models of global dust storm onset and evolution, we know that at some size, duration, and optical depth the background atmospheric thermal and dynamical state does become sensitive to the optical depth perturbations associated with the storm (e.g., Wilson, 1997; Newman et al., 2002). In this section, we explore the response of the atmosphere to imposition of regional scale storms, as defined in Section 2. We do this by prescribing regional dust storms over areas that include locations 1 and 2 from the local storm study (western Hellas and western Chryse, respectively; see Fig. 2 and Table 2). For both locations, perturbation dust optical depths are imposed within areas of 31 × 15 gridpoints (62° longitude by 30° latitude). This corresponds to an area of over 50 times greater than that imposed for the local storms.

For analysis purposes, the storm center definitions remain unchanged from those used for the local storms, but the large latitudinal variations across the storm areas means that an extended halo cannot be used because latitudinal variations in the fields would swamp the natural time variation and the storm-induced variations. Instead, several different locations exterior to the storms, defined by a square region 3 × 3 gridpoints in size (6° longitude by 6° latitude), have been used and their locations are specified within the analysis, as described below.

We show results from both simulated regional storm locations, since some of the regional storms (at higher optical depth) do generate a consequential feedback on aspects of the circulation. For the chosen simulation period, the location 1 site is nearer the upwelling region of the tropical overturning ("Hadley") circulation, while location 2 is nearer the downwelling region, and thus the two storms have rather different phenomenological character. However, we again note that the purpose of this study is to ask whether storms of any given size consequentially modify the circulation, with the phenomenological description of how the response develops being secondary.

4.1. Regional, long duration (10.5 sol) storms

The near-surface and mid-level air temperatures and winds during the last sol of a 10-sol regional storm imposed over the western Hellas region (location 1) are shown in Fig. 11. The area of the imposed storm is indicated by the overlain box. Optical depth cases of τ=3, 10, 30, and 200 are shown (only this set of simulations use an upper bound of optical depth of 200 instead of 250). The simulations are summarized in Table 1. The imposed regional storm overlaps the area of the imposed local storm shown in Section 3, but is also of interest because of the interaction of the region with the growing CO_2 ice cap and because of the observed importance of the western Hellas region for the initiation of the 2001 and 2007 global storms (Strausberg et al., 2005; Wang and Richardson, 2015).

The near-surface air temperatures at 2 PM show the same significant cooling as the local storms (Section 3) as the dust optical depth is increased. This results from the same shading of the surface and lower atmosphere at high optical depths. Note that the temperature contrast across the edge of the storm can be very large when the optical depth is high. This very large contrast is reasonable when compared with the very significant decrease in the daily maximum air temperatures measured by Viking Lander 1 during both 1977 global storms (e.g., Ryan and Henry, 1979). The dynamical response at synoptic scales of the regional storm is a little different from those of the local storms, however. While the local storms developed near-surface weak outflow at high opacity, the regional storm develops consistent, but weak, inflow, though

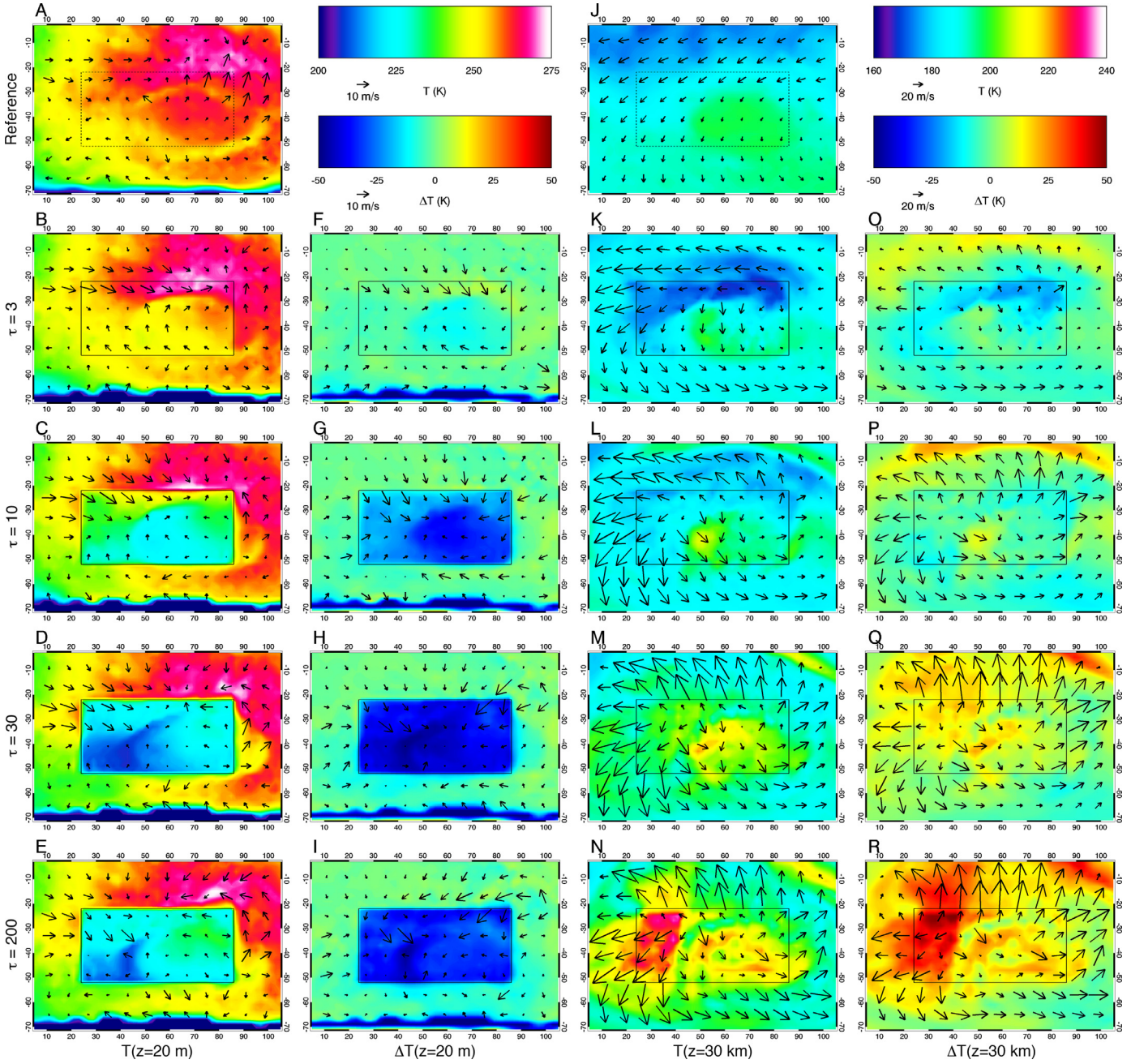

Fig. 11. Same as Fig. 5, except showing differences in the location 1 10.5-sol regional storm simulations at an approximate local time of 2 PM (at the center of the storm) on the final sol of the simulated storm, i.e., the thirteenth sol of the overall simulation. Rectangular black boxes overlain in the center of each map show the areal extent of the imposed regional storm. Note the change in color scales.

without a clear spatial pattern. This flow pattern suggests inflow and upwelling at low levels within the storm, whereas for the local storms the cold air mass within the storm center was instead collapsing and outflowing at the surface. This wind field perturbation extends significantly beyond the edge of the prescribed storm area.

At higher altitudes, the 2 PM air temperature is increased above the reference case for all simulations, but with significantly warmer temperatures at larger optical depth. The wind field at higher altitudes is increasingly perturbed as the optical depth increases. In all cases a divergent perturbation flow develops with associated anti-clockwise (anti-cyclonic) motion about the storm. The combination of the high and low altitude flow perturbations suggests that the full three-dimensional perturbation flow field is associated with low-altitude convergence, upwelling within the storm, and with divergence and outflow at high altitudes. Note that the air arising from near the surface is significantly cooler than that at higher altitudes (the atmosphere is strongly stably stratified) for the higher opacity cases and as such is being “pulled” upwards from above (by a high-altitude induced outflow) rather than being buoyantly “pushed” upwards from near the surface.

Fig. 12 shows the signature in the thermal and dynamical state of the atmosphere several sols after the storm has ended. At low altitudes, the rapid response of the surface to local radiative balance quickly damps the large amplitude of the perturbations seen during the storm, but residual deviations of several K remain, both within and exterior to the area of storm imposition. This seems especially evident along the southern edge of the area shown in

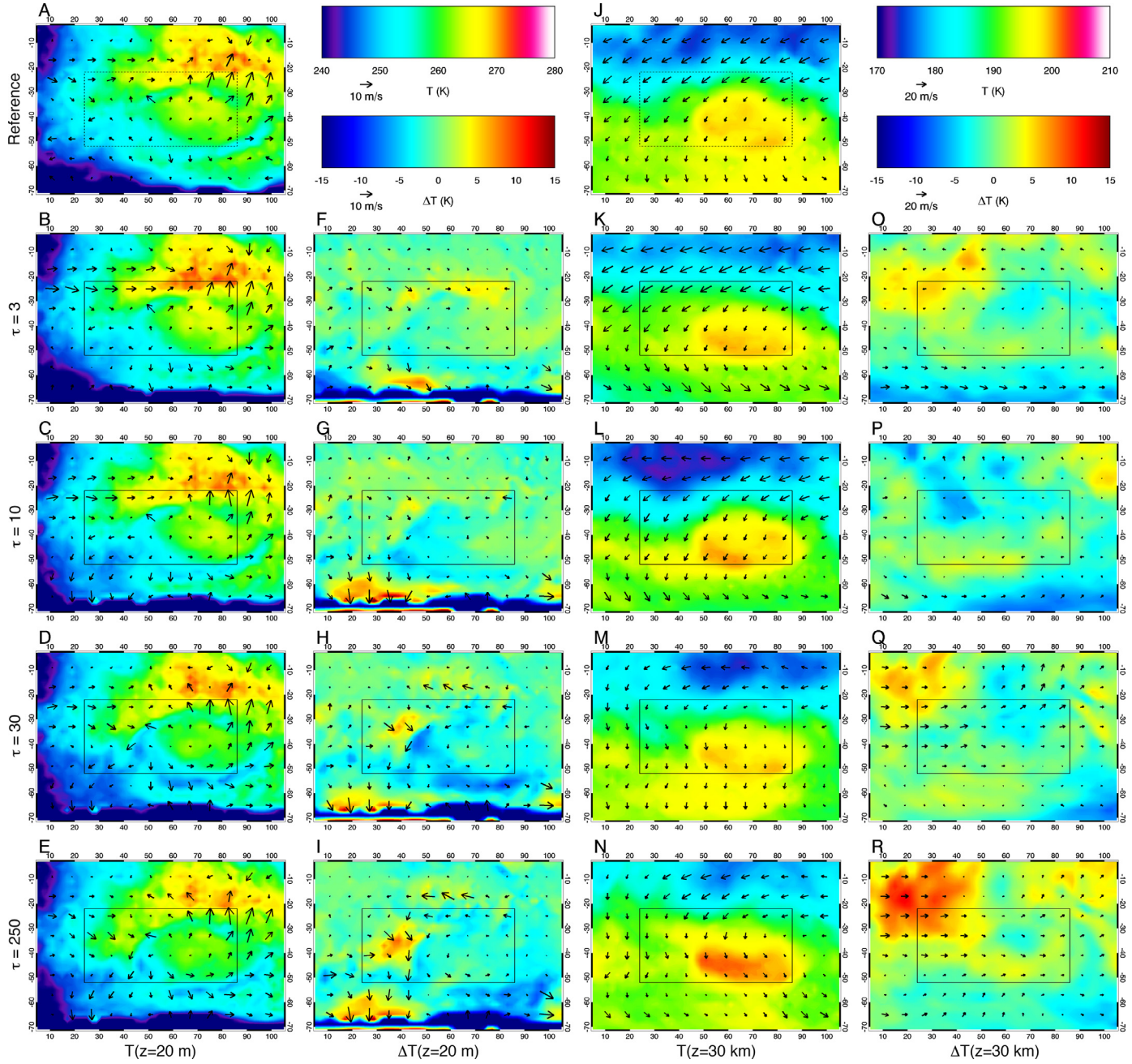

Fig. 12. Same as Fig. 11, except showing an approximate local time of 2 PM (at the center of the storm) 2 sols after the storm has ended, i.e., the fifteenth sol of the overall simulation. Note the change in color scales.

the map panels where the storm appears to have modified the cap edge distribution of CO_2 ice. The wind field perturbation at low altitudes has also become mildly anti-cyclonic (anti-clockwise), due to the termination of the thermally induced surface low pressure system after the storm cessation.

At higher altitudes, the thermal structure remains very significantly perturbed 2 sols after the end of the storm. The differences are visible as large-scale perturbations in the meridional thermal structure and with most of the heating (relative to the non-storm reference case) being at latitudes away from the area of storm imposition. This heating must therefore be associated with dynamical rather than radiative processes.

The influence of a long duration, regional storm imposed over western Chryse (location 2), both during and after the 10-sol period of storm imposition, is shown in Figs. 13 and 14, respectively. The Chryse storm is interesting in that it is forced within the context of the strong polar jet. The zonal mean structure of the polar jet in the non-storm reference can be seen in Fig. 17a. The general pattern of thermal perturbation during the storm (Fig. 13) at both lower and higher altitudes is generally similar to that of the storm near Hellas: cooling at low altitudes resulting from shading; heating at higher altitudes; and lower altitude convergence and higher altitude divergence. However, there are clearly some more complex patterns of interaction with the jet at higher altitudes. The simulations generate a significant warming of the atmosphere poleward of the jet core. The perturbation higher altitude wind fields show a net meridional flow poleward across the jet.

The influence of all four storm strength cases upon the polar jet at upper levels is evident 2 sols after the end of the storm (Fig. 14). In all cases, the polar air mass is cooled relative to the storm-free

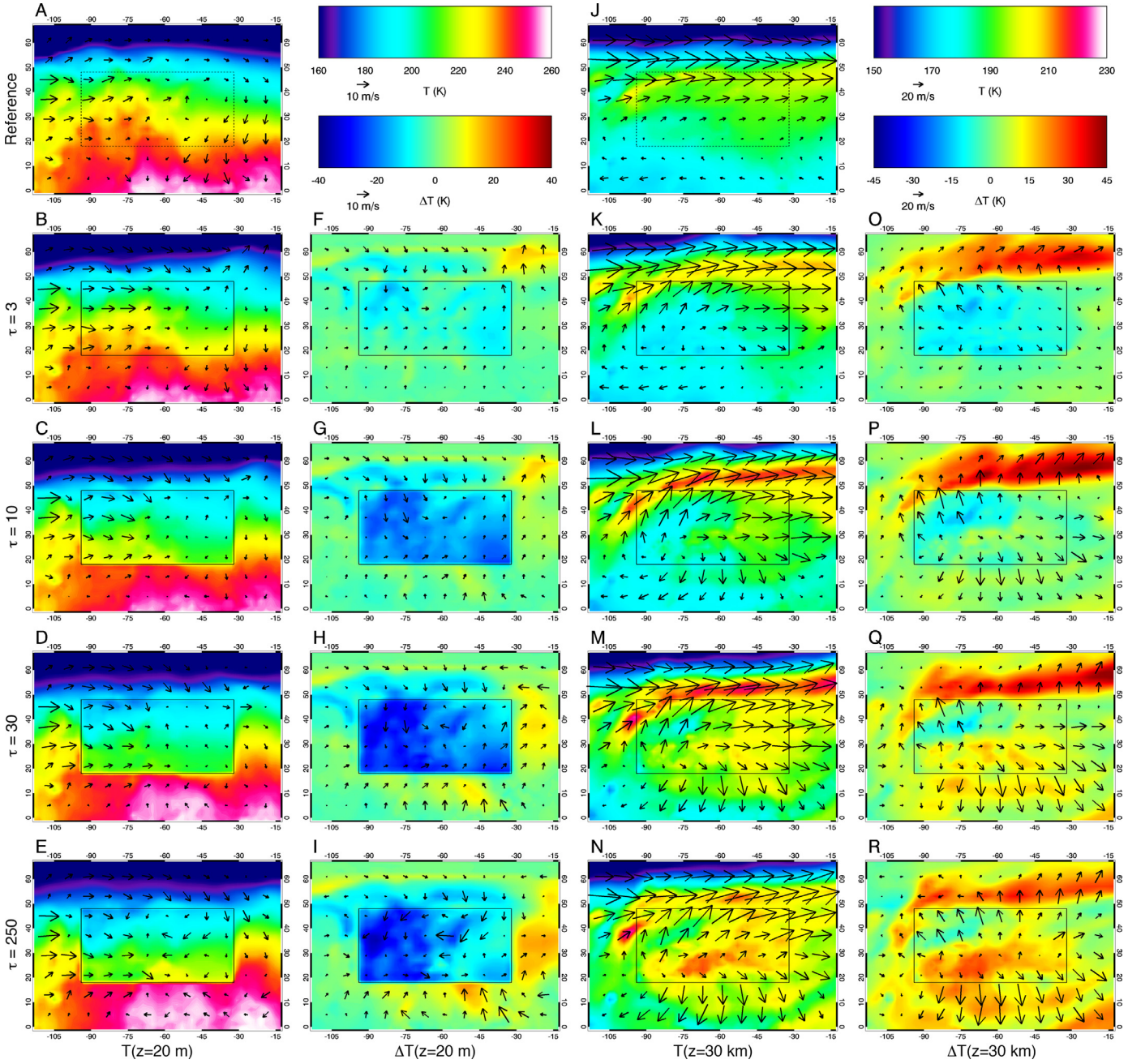

Fig. 13. Same as Fig. 5, except showing differences in the location 2 10.5-sol regional storm simulations at an approximate local time of 2 PM (at the center of the storm) on the final sol of the simulated storm, i.e., the thirteenth sol of the overall simulation. Note the change in color scales.

reference case and the jet is deflected further to the south. This represents a "rebound" of the jet relative to its poleward deflection during the storm and also results in a strong wave forcing along the jet. At lower altitudes, there also remains a cooling effect of the storm.

In summary, Figs. 11 to 14 show that, unlike the local storms, the regional storms are able to modify the atmosphere at a significant distance from the area directly experiencing an increase in dust optical depth while the storm is occurring, and that this persists for several sols even after radiative heating is removed. Although the radiative forcing reverts to be equivalent to the non-storm reference case immediately upon the termination of the imposed storm, the atmospheric dynamical and thermal state has been sufficiently affected so as to require time to relax back to the unperturbed case.

Quantitative and time-evolving information on the lower and higher altitude air temperatures from the long duration regional storm imposed at location 1 (Hellas) is shown in Fig. 15. These plots also show the environmental variance in the non-storm reference case (solid line) against which the magnitude of deviations of the storm cases can quantitatively be compared, as was also done for the local storms in Section 3. However, rather than comparing deviations and natural variability over a halo surrounding the storm (as was done for the local storms), for the regional storm we compare them at two different storm-exterior 3 × 3 gridpoint sites, northeast and northwest of the storm, at locations indicated in the Fig. 15 caption.

As with the local storms, near-surface air temperatures within the storm are significantly modified relative to the non-storm reference case. However, with the regional storms, near-surface tem-

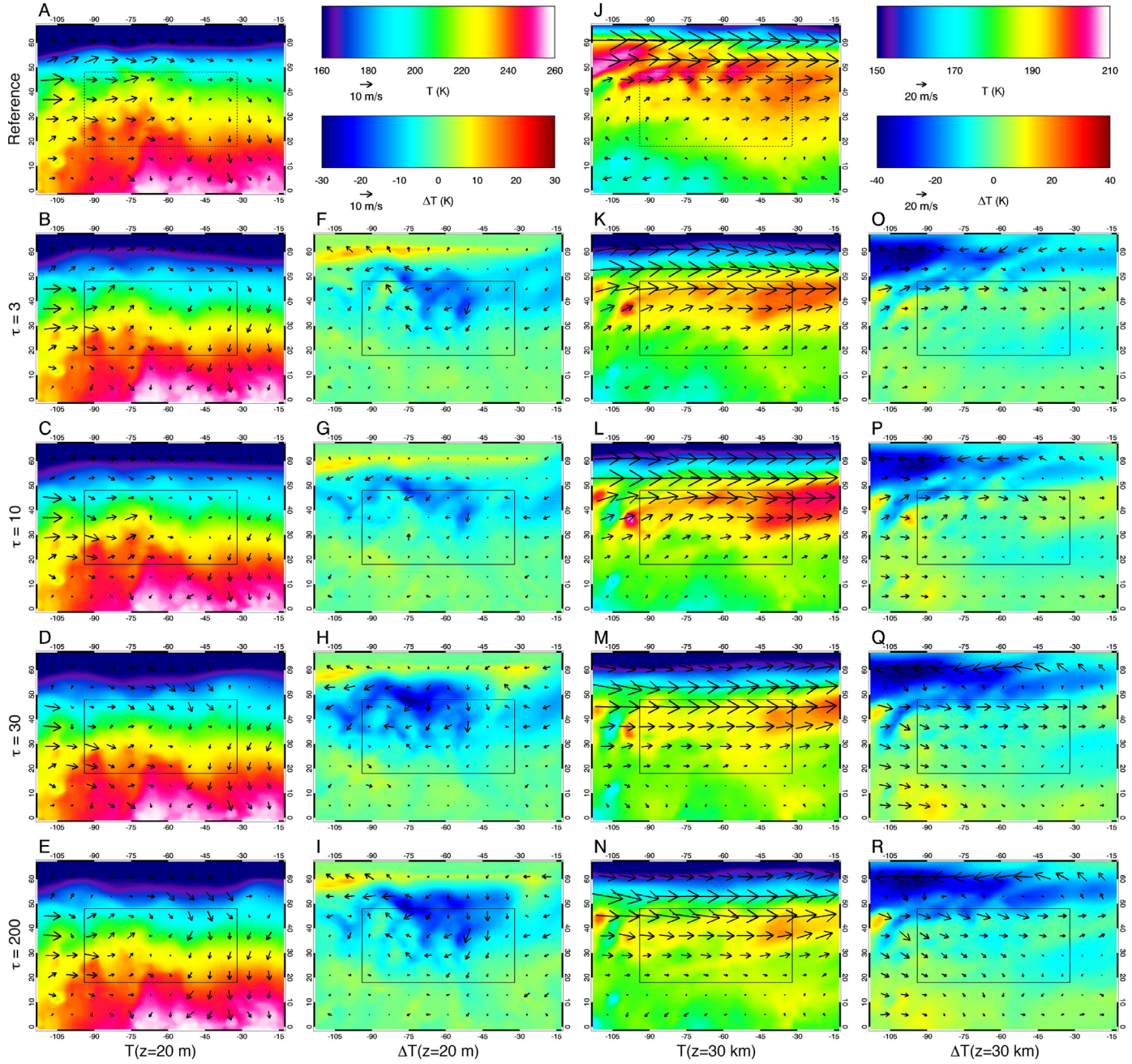

Fig. 14. Same as Fig. 13, except showing an approximate local time of 2 PM (at the center of the storm) 2 sols after the storm has ended, i.e., the fifteenth sol of the overall simulation. Note the change in color scales.

peratures exterior to the storm are also significantly modified, even in the lowest optical depth case. As suggested by examination of the air temperature maps at a fixed instant of time (Fig. 14), the deviation of the near-surface air temperature from the unperturbed non-storm reference case persists many sols after the termination of the storm, though the existence and magnitude of the perturbation is a strong function of relative location and imposed storm strength. This likely reflects the fact that regional storms influence the larger-scale and longer-lived circulation by modifying existing synoptic circulation systems. Depending on where in particular the storm is imposed relative to these circulation systems, the storm will have a varying ability to influence them. For the purposes of the current study these details do not matter; what is important is that the long-duration regional storms have a demonstrated capability to modify the background circulation, both at significant distances from the area actually heated by the atmospheric dust and for a significant time interval after the heating has been removed. The distal atmosphere clearly "notices" the long duration regional storms whereas it did not notice the local storms discussed in Section 3.

Surface wind stress perturbations within and exterior to the imposed storms are interesting because of the implications for further wind-stress dust lifting. The temporal evolution of perturbation wind stresses both at the storm center and the exterior sites mentioned above are shown in Fig. 16. In all areas, the deviations in wind stress between the storm cases and the reference case are larger than the natural variability at those locations in the reference case during the storm interval. Wind stress deviations in ex-

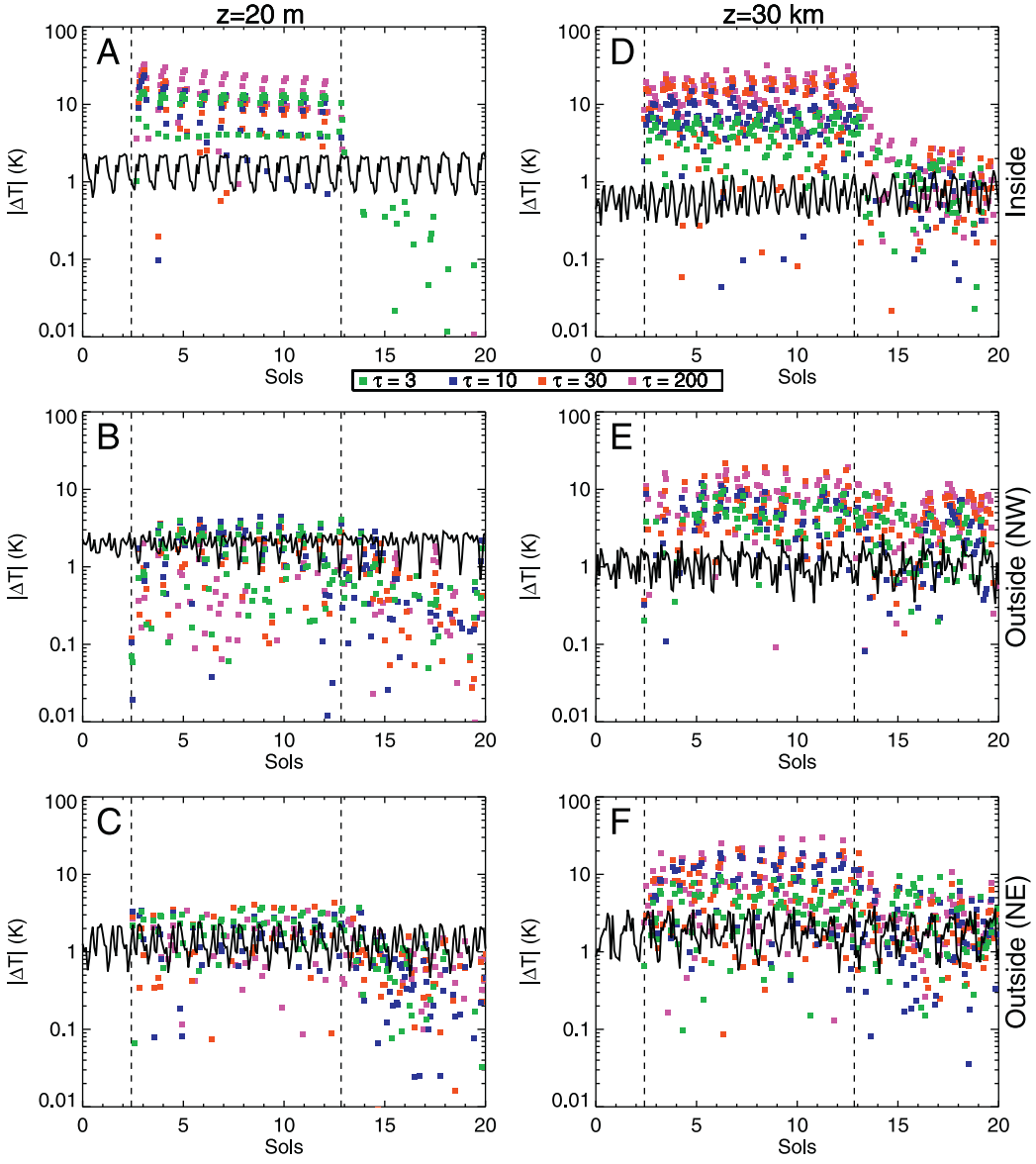

Fig. 15. The absolute value difference of temperature (colored squares) in location 1 10.5-sol regional storm simulations relative to the storm-free case during the course of the simulations. The left column (A–C) shows near-surface (approximately 20 m altitude) air temperature differences, while the right column (D–F) shows mid-atmosphere (approximately 30 km altitude) temperature differences. For the top row (A,D) the panels show the difference of the central gridpoint of the 31 × 15 gridpoint area of the simulated storm area. For the second and third rows (B–C,E–F), differences are calculated at gridpoints outside the storm area. For the second row (B,E), the gridpoint is two gridpoints north west of the northwest corner of the storm location, while for the third row (C,F), the gridpoint is two gridpoints northeast of the northeast corner of the storm location. In each panel, the vertical dashed line shows the starting and ending times of the prescribed regional storms, while the solid line shows the standard deviation in the reference simulation of a 9 (3 × 3) gridpoint area centered on the gridpoint of interest in each row, i.e., the central gridpoint of the storm in (A,D), and the three points outside the storm area in (B–C,E–F). In all panels, the color of the square indicates the optical depth of the storm in the simulation (see key in center of figure).

cess of background variability continue for several sols after the end of the storm.

To complete the picture regarding how the regional storms influence the synoptic-scale atmosphere, we show in Figs. 17 and 18 meridional cross-sections of the zonal-mean zonal wind and its deviation from the non-storm reference state several sols after the termination of the applied storm. The Hellas (location 1) storm is shown in Fig. 17, while the Chryse (location 2) storm is shown in Fig. 18. The zonal wind is easily interpretable in terms of the latitudinal gradient in the atmospheric temperature and vice versa via the thermal wind relationship.

Fig. 17 shows the zonal-mean zonal wind response to the regional storm in Hellas (location 1). Here the heating is applied within the southern (summer) hemisphere upwelling branch of the mean overturning circulation. The result is to weaken both the easterlies over the equator at mid-altitudes and the westerly polar jet, especially on its equatorward side. The result is a narrowing of the westerly polar jet and a shifting of its centroid towards the pole. There is also a significant warming of the winter polar atmosphere. Modeling of the response of the general circulation to the widespread dust forcing associated with global dust storms has shown that the overall increase of the meridional overturning ("Hadley") circulation is directly linked to winter polar warming and the decrease in the strength of the polar jet (e.g., Wilson, 1997). Clearly even the more spatially confined dust forcing used in our regional storm simulations produces a qualitatively similar response. The increase in the poleward transport in the overturning circulation is accomplished at higher alti-

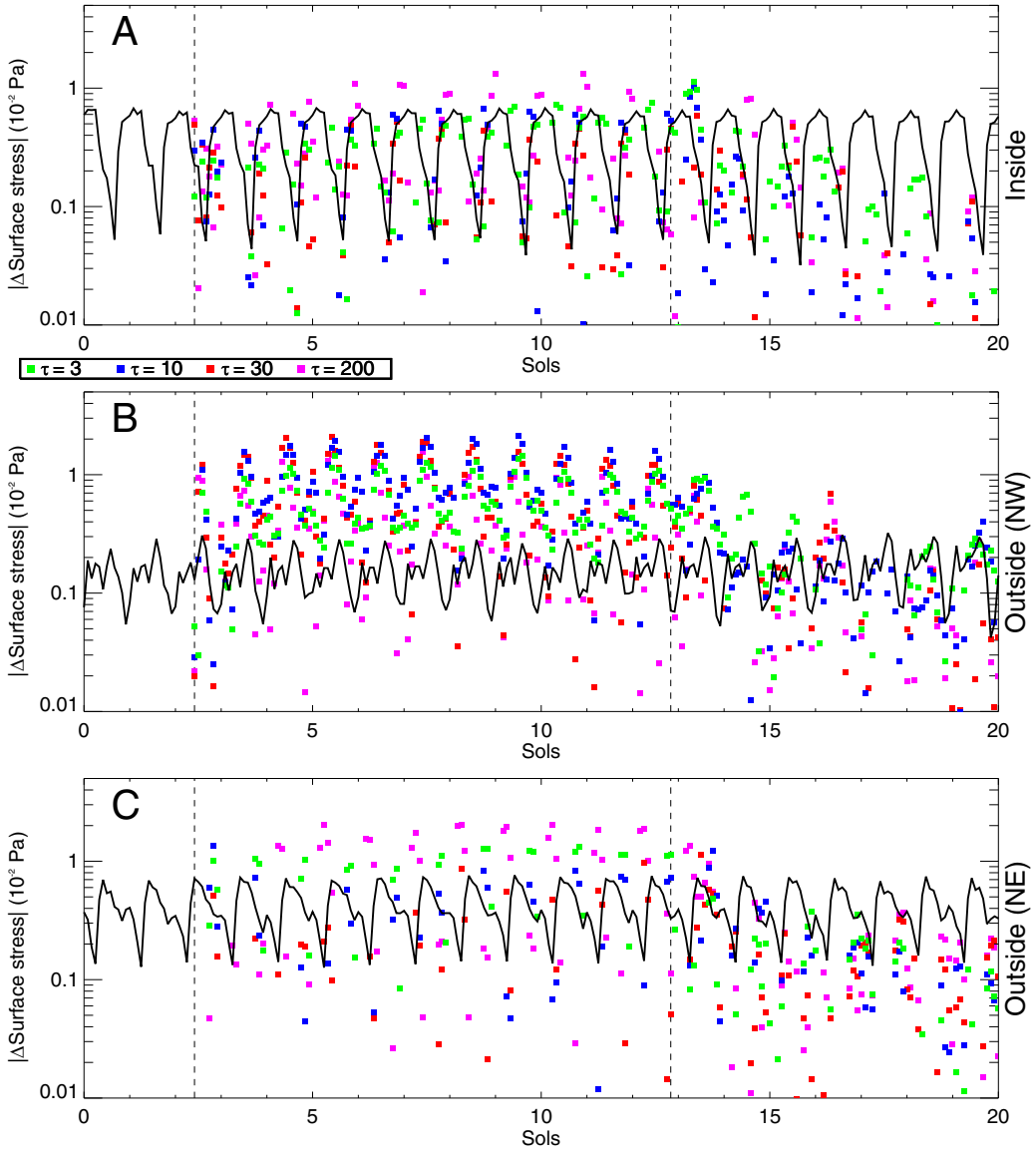

Fig. 16. Similar to Fig. 15, except showing absolute value differences in surface wind stress. The rows represent the same physical location as used in Fig. 15.

tudes than the peak in the non-storm reference case, as can be inferred from Fig. 17 from the strong decrease in westerlies (i.e., the stronger negative wind perturbations) in the northern hemisphere above 40–50 km in storms of optical depth of $\tau \geq 10$.

Fig. 18 shows, for the Chryse storm, the more complex influence of a regional storm applied within the northern (winter) hemisphere downwelling branch of the overturning circulation. The polar jet is slowed and shifted poleward more significantly than for the Hellas storm (for equivalent optical depths). However, the strong negative wind perturbations (i.e., weakening of jet westerlies) that developed throughout the northern hemisphere at levels above 40 km for the Hellas storm only appear above 70 km or so for the Chryse storm. This suggests much less strengthening of the overturning circulation for the winter hemisphere storm in Chryse than for the summer hemisphere storm in Hellas. The easterly acceleration, however, extends deeply into the southern hemisphere for the Chryse storm, suggesting a more hemispherically consistent (south-to-north) acceleration of the flow near the model top. Combined with increasing westerlies in the southern high latitudes, the effect of the Chryse (winter) storm is to make the circulation more hemispherically symmetric, i.e., to push the meridional circulation toward a more equinoctial (as opposed to solsticial) pattern.

4.2. Regional, short duration (1.5 sol) storms

The simulations examined to this point have shown that while local storms (of order 10^5 km^2) do not significantly perturb the atmosphere beyond the area directly heated by suspended dust and have no significant impact on the atmosphere after storm cessation, regional storms applied for multiple sols over areas of order 10^6 km^2 have both a widespread and lasting impact. In this section, we briefly examine an intermediate case of a regional storm applied for 1.5 sols, i.e., the same length of time as used for simulating the typical local storms. The results of these simulations are not shown here but are provided in the supplementary materials.

As with all the various storm cases (of different areal extents and durations) already shown in this study, the near-surface air temperatures are cooled due to dust shading of the surface while the storm is active. Exterior to the storm, however, there is little signature in either the temperature or wind fields at low altitudes during the storm. This result extends to the period after storm ces-

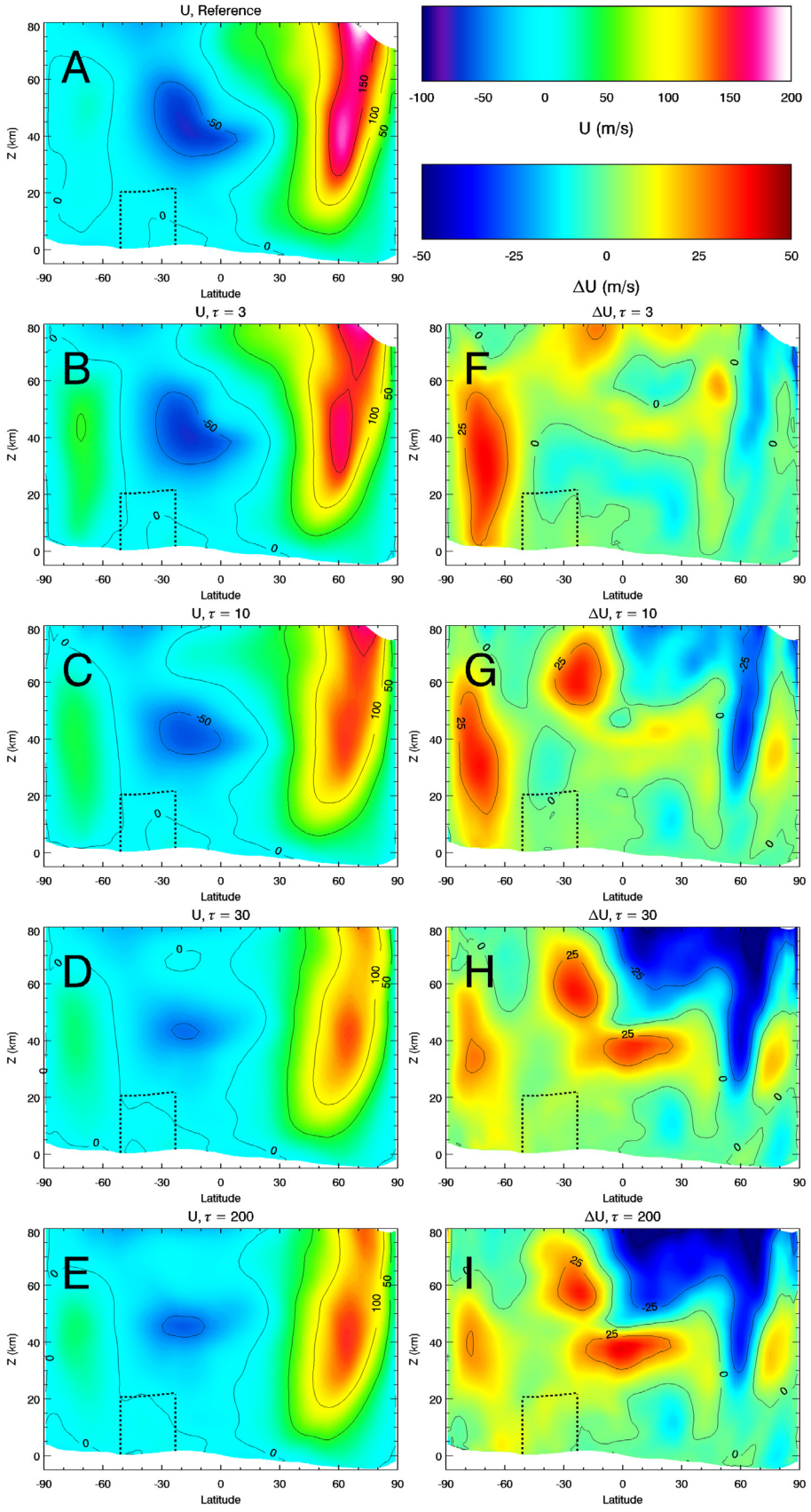

Fig. 17. Zonal-average zonal winds (A–E, left column) and differences (F–I, right column) of those zonal-average zonal winds from the reference (storm-free) simulation in the location 1 10.5-sol storm simulations as a function of latitude and altitude. Model output is shown from the tenth sol after commencement of the storm, i.e., the thirteenth sol of the overall simulation, and results at each longitude have also been averaged over that entire sol to remove any residual tidal signature in the zonal averages. (A) Reference (storm-free) simulation; (B,F) τ=3 simulation; (C,G) τ=10 simulation; (D,H) τ=30 simulation; (E,I) τ=200 simulation. At the top of the second column, color scales for zonal winds (upper) and zonal wind differences (lower) are shown. Dashed lines in each panel show the latitudinal and vertical extent of the simulated regional storm area.

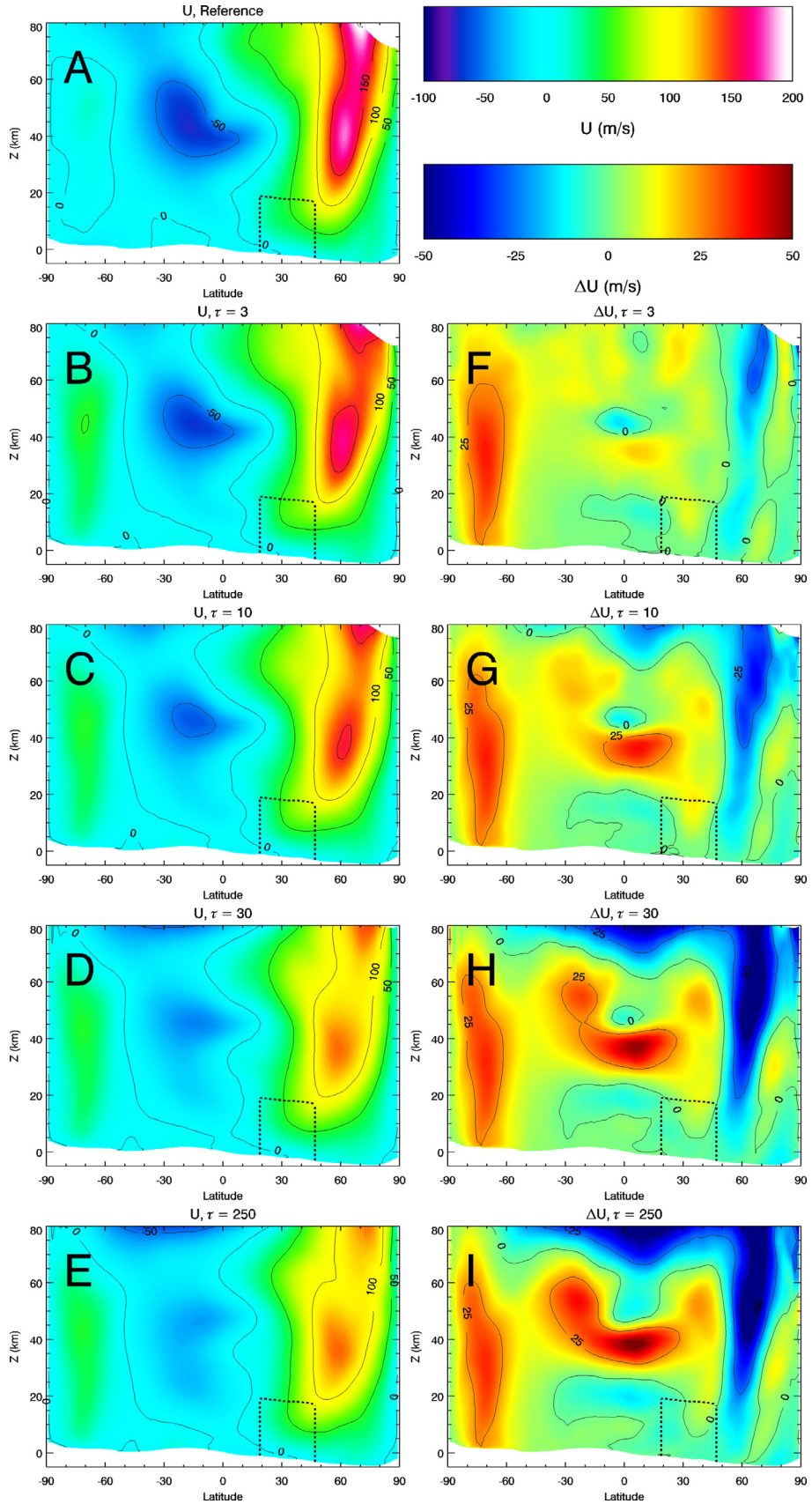

Fig. 18. Same as Fig. 17, except for the location 2 10.5-sol regional storm simulation, and at an equivalent time during the storm (i.e., the tenth sol of the storm, the thirteenth sol of the overall simulation).

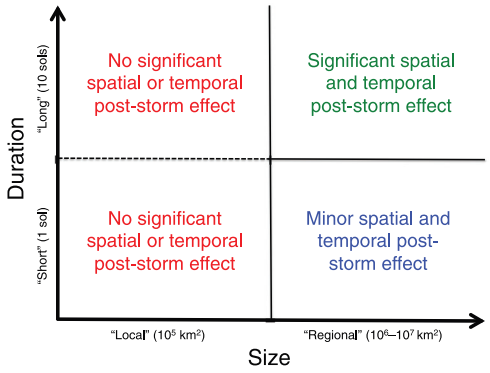

Fig. 19. Schematic diagram showing two dimensions of storm size and storm duration of the phase space of Martian dust storms to illustrate broad regimes of feedback effects for the different storm types examined in this study. A third, orthogonal, phase dimension of storm optical depth is not shown, as it only acts as a roughly monotonic intensifier of these effects when they occur, without significantly altering the nature of the regimes.

sation as well. At higher altitudes, the storms generate a heating interior to the area of imposed optical depth increase while the storm is active. After the storm cessation, all of the storm cases show a modest cooling of the high (poleward) latitudes, corresponding to a slight cooling of the post-storm winter polar vortex on its equatorward side. Surface wind stress variations due to the storm are only in some areas slightly larger the natural variability of the non-storm reference case. Finally, the influence of the Hellas and Chryse storms on the zonal mean circulation is in the same sense as that described for the long duration (10.5 sol) regional storms, but with much smaller magnitudes.

In summary, these results suggest that, unlike the case for the longer duration regional storms, short-lived regional storms have only a very weak impact on air temperatures, high altitude winds, and surface wind stresses. Thus, it is evident that, even if applied over large length scales, if dust forcing does not last for some threshold number of sols (between 1.5 and 10) it does not significantly modify the distal atmosphere, nor are the effects long-lasting in the region of the storm itself once the heating has ceased.

5. Discussion and conclusions

In this study, we have explored a range of spatial and temporal scales of dust storms, motivated by observations, over which we searched for the occurrence of meaningful atmospheric dynamical response to storms. While experiments have previously been conducted with the MarsWRF GCM using a fully interactive dust cycle (Newman and Richardson, 2015), this study was designed to isolate the synoptic response solely to the prescription of static dust storm thermal forcing. The model was used to specifically investigate whether storm heating alone has the potential to generate a larger scale atmospheric response that could generate increase dust lifting either close to or at a distance from the initial storm, or precondition the atmosphere for future storm growth.

Our results show that imposed heating perturbations on the scale of observed local dust storms (of order 10^5 km^2 and about 1 sol) are not sufficient to cause significant atmospheric response outside the area of imposed storm heating. Significance is defined via comparison with the modeled natural variability of an otherwise identical model simulation but without any additional heating from an imposed dust storm. In other words, heating from imposed local storms does not change the thermal or dynamical state of the atmosphere beyond the area of direct forcing by amounts larger than the normal environmental variance. This result is applicable to six different areas sampled across the globe and to a broad range of optical depths.

We investigated whether the duration of imposition of local storms and their consequent heating influenced the atmospheric response beyond storm cessation by applying heating for 10.5 sols rather than the default 1.5 sol time scale of most local storms. This set of experiments was designed to test the hypothesis that the influence of the local storm was not allowed to develop for long enough relative to the radiative time constant of the atmosphere, approximately 1–2 sols (Goody and Belton, 1967). The model results suggest that the duration of storm imposition is not significant at the length scales of local storms. During the period of storm forcing, the magnitude of the interior and exterior thermal and dynamical perturbations were similar to those that developed within the 1.5-sol duration storms. After cessation of the 10.5-sol storms, the atmosphere returned to its pre-storm state as rapidly as the reversion that followed cessation of the 1.5-sol storms.

The mesoscale dynamics within local storms have previously been investigated by Rafkin (2009) and Spiga et al. (2013). Our experiments were run at synoptic scales and thus did not capture mesoscale systems; however, they do shed some light on local storm internal dynamics. Our results suggest that there is "buoyant collapse" in the lower reaches of the storms with consequent near-surface outflow. The modeled local storms also demonstrate a vertical segregation of buoyancy, with shading and cooling at lower altitudes being compensated for with higher altitude ("cloud deck") heating and generation of positive buoyancy. This vertical structure is qualitatively similar to that generated in the detachment of "rocket" dust storms (Spiga et al., 2013), although our chosen model resolution and focus on non-advective dust does not allow us to comment on the potential strength of the vertical transport of dust.

The next category of storm was examined by increasing the storm area to over 10^6 km^2 and the duration to 10.5 sols, both typical of regional storms. At these scales, the regional storms created significant perturbations to the thermal and dynamical structure both beyond the area of thermal forcing imposition and after cessation of the thermal forcing. The precise nature of the perturbations depended on location, both the location relative to the storm center and the absolute geographical location, and would almost certainly differ for different seasons. However, the important point for this paper is that regional, long-lived storms have the potential to dramatically change the atmospheric structure outside of the location and period of imposed optical depth and therefore that storm feedback associated with the direct thermal and dynamical impact of the storm (rather than due to aerosol lateral mixing or advection) is possible for this category of storms. The isolation of this mechanism would not have been possible in a more complex experimental setup where radiative-dynamical-advective interactions would have become blurred and potentially confused.

The regional storms not only influenced the atmosphere in the surrounding region outside the storm, but also modified the global circulation. The ability of large-scale changes of atmospheric dust to modify the general circulation is well-known (e.g., Haberle et al., 1982; 1993; Murphy et al., 1995; Wilson, 1997; Newman et al., 2002; Basu et al., 2004; Kahre et al., 2006). The regional storms simulated for this study, at Ls=220°, show a more complex response than the direct intensification of the meridional circulation that results from global optical depth increases. The summer hemisphere Hellas (location 1) storm generates an increasing intensification of the overturning circulation with increasing optical depth. The winter hemisphere Chryse (location 2) storm is more complex, with both a weakening of the polar jet and of the mean overturning circulation. Instead of accelerating the solstice-like mean circulation that exists in the reference case, the Chryse storm tends to oppose the circulation and revert the atmosphere

to a more equinox-like state. The reason for this difference is that, in the Hellas storm, the heating is imposed in the region containing the upwelling branch of the Hadley cell, whereas for the Chryse storm the heating is imposed in the region containing the downwelling branch. Significant thermal perturbation signatures at a distance from the location of imposed optical depth enhancements are noted in both cases, which is consistent with spacecraft observations that show a thermal response at great distance from the location of long-duration regional dust storms (e.g., Kass et al., 2016).

Our results suggest that when dust heating is applied for many sols, a very significant transition in impact on the atmosphere exists for spatial scales between 10^5 and 10^6 km^2. We further examined whether there was an analogous temporal threshold, i.e., whether long storms would produce a greater response than short storms. The result was that there was no significant distal or long-lasting response to local storms on either time scale, but there was a threshold for regional storm response between 1 and 10 sols. We can speculate about the reasons for both the time scale and length scale threshold for creation of distal and long-lasting storm response to heating. We have already mentioned that the time scale threshold appears coincident with the radiative timescale of the lower atmosphere, where the application of heat for long enough may allow dynamical processes to become competitive with the re-radiation of heat to space. For the dynamical length scale threshold, there are two potential physical explanations. First, the threshold in the length scale is consistent with the longest scale that can plausibly be advected in one sol and thus may represent the minimum scale that can be sustained against advective dissipation. Second, the threshold is close to the Rossby radius of deformation, which provides a gauge of the smallest length scale at which coherent synoptic scale structures can be sustained.

Based on all of the simulations performed in this study, we thus conclude that thresholds for significant distal and long-lasting response exist when the storm is larger than a threshold area between about 10^5 to 10^6 km^2 and lasts longer than a threshold duration between 1 and 10 sols. Empirically, it may be possible to refine the location of these spatial and temporal thresholds through many further simulations, but it is unclear how sensitive the precise locations (or widths) of these thresholds would be to geographical storm location (examined to a limited extent here), seasonality (not examined here), and even optical depth. Despite the relatively limited range of phase space parameters examined here, it should be noted that the super-set of ensembles used already exceeds 200 individual simulated cases. The range of storm optical depths already examined here indicate that, at least for optical depths greater than or equal to 1, increasing the dust storm strength acts only to intensify results roughly monotonically, and does not change the qualitative results. Fig. 19 shows a generalized schematic of the influence of the different classes of storms examined in this study based on storm size and duration.

Although not shown, we completed the full range of simulations (location, size, and duration) presented in this paper but with the increase in dust optical depth spread through the full vertical extent of the atmosphere following a Conrath profile. Because of the functional form of the Conrath profile, this is equivalent to a storm capped at about 45–70 km altitude (depending on latitude). These results effectively repeat those shown already in the paper, in the sense that local and short duration regional storms do not significantly perturb the atmosphere above the natural background variability. The results also show that long duration regional storms modify the large-scale structure. The details of the modification of the circulation in these cases with deeply spread dust are different from those cases where the dust is limited to a vertical extent of 20 km. However, the differences are not significant to the conclusions presented in this work.

The central implication of this study is that the vast majority of local dust storms on Mars likely lie in a size and duration regime below the thresholds necessary to trigger their growth to the next category scale along the dust storm cascade via the production of a distal and long-lasting atmospheric response. Implicit in this conclusion is the concept that dust storms exist in one of a number of different size states that are differentiable on the basis of their fundamental growth mechanisms, which in turn depend upon their size and history. Full growth from local to global scales involves the crossing of several different size and duration thresholds that activate different feedback systems within the local, regional, and global atmosphere. Our results are preliminary in the sense that advection of dust to other locations might provide an additional means for feedback growth that is not considered here. However, the extent of dust advection over a diurnal timescale with continuous application of typical lower atmosphere wind speeds is of order 1000 km, although with tidal turning, net advection distances would tend to be much less, around 200 km (and thus only one or two extra gridpoints at the resolution of the simulations used here). It thus remains to be tested whether the advection of dust, and its impact on heating and circulation distal to the storm, facilitates local storm growth. It is also possible that, while a prescribed uniform increase in dust loading does not appear to enhance wind stresses (and hence lifting) within or at the periphery of a local storm, micro/mesoscale processes not captured here may be able to do so. However, the present study demonstrates unambiguously that thermal and dynamical perturbations alone cannot grow local storms.

Considering only the thermal and dynamical response, our results show that local storms do not generate larger-scale external feedbacks, i.e., they do not induce significant dynamical flows exterior to the storm. This suggests another key result of this study, that if only thermal and dynamical processes are important, local storms are a distinct category of event definable by their dependence for creation upon circulations at scales larger than themselves, and do not have access to growth mechanisms available to regional (and global) storms. The size, evolution, and duration of local storms would then be a function purely of externally imposed conditions: the size and duration of the surrounding wind system (e.g., the area and period of winds experienced due to tidal or baroclinic wave amplification (Wang et al., 2003), or the constructive interference of tidal, cap, and slope flows (e.g., Toigo et al., 2002) and the surface availability of loftable dust. If so, then only when the coincidence of these externally imposed conditions generates a storm of sufficient size and for sufficient duration (i.e., longer-lived regional storms) would exterior storm-induced flows enable the possibility of further amplification of the storm to planet-encircling or global scales.

Acknowledgements

This work was supported by the NASA Mars Data Analysis Program, Grant NNX13AK80G. We also thank Nicholas Heavens and Richard Zurek for their generous assistance in improving this paper.

Supplementary material

Supplementary material associated with this article can be found, in the online version, at doi:10.1016/j.icarus.2017.11.032.

References

Ayoub, F., Avouac, J.-P., Newman, C.E., Richardson, M.I., Kucas, A., Leprince, S., Bridges, N.T., 2014. Threshold for sand mobility on Mars calibrated from seasonal variations of sand flux. Nat. Commun. 5, 5096. doi:10.1038/ncoms6096.

Basu, S., Richardson, M.I., Wilson, R.J., 2004. Simulation of the Martian dust cycle with the GFDL Mars GCM. J. Geophys. Res. 109 (E18), E11006.
Briggs, G.A., Baum, W.A., Barnes, J., 1979. Viking Orbiter imaging observations of dust in the Martian atmosphere. J. Geophys. Res. 84, 2795–2820.
Cantor, B.A., James, P.B., Caplinger, M., Wolff, M.J., 2001. Martian dust storms: 1999 Mars Orbiter Camera observations. J. Geophys. Res. 106 (E10), 23653–23687.
Colburn, D.S., Pollack, J.B., Haberle, R.M., 1989. Diurnal variations in optical depth at Mars. Icarus 79, 159–189.
Conrath, B.J., 1975. Thermal structure of the Martian atmosphere during the dissipation of the dust storm of 1971. Icarus 24, 36–46.
Goody, R.M., Belton, M.J.S., 1967. Radiative relaxation times for Mars: a discussion of Martian atmospheric dynamics. Planet. Space Sci. 15, 247–256.
Guo, X., Lawson, W.G., Richardson, M.I., Toigo, A.D., 2009. Fitting the Viking lander surface pressure cycle with a Mars General Circulation Model. J. Geophys. Res. 114. doi:10.1029/2008JE003302.
Guzewich, S.D., Talaat, E.R., Toigo, A.D., Waugh, D.W., McConnochie, T.H., 2013. High-altitude dust layers on Mars: observations with the Thermal Emission Spectrometer. J. Geophys. Res. 118 (6), 1177–1194. doi:10.1002/jgre.20076.
Guzewich, S.D., Toigo, A.D., Kulowski, L., Wang, H., 2015. Mars Orbiter Camera climatology of textured dust storms. Icarus 258, 1–13.
Guzewich, S.D., Toigo, A.D., Wang, H., 2017. An investigation of dust storms observed with the Mars Color Imager. Icarus 289, 199–213. doi:10.1016/j.icarus.2017.02.020.
Haberle, R.M., Leovy, C.B., Pollack, J.B., 1982. Some effects of global dust storms on the atmospheric circulation of Mars. Icarus 50 (2–3), 322–367.
Haberle, R.M., Pollack, J.B., Barnes, J.R., Zurek, R.W., Leovy, C.B., Murphy, J.R., Lee, H., Schaeffer, J., 1993. Mars atmospheric dynamics as simulated by the NASA Ames General Circulation Model: 1. The zonal-mean circulation. J. Geophys. Res. 98 (E2), 3093–3123.
Heavens, N.G., 2017. Textured dust storm activity in Northeast Amazonis Southwest Arcadia, Mars: phenomenology and dynamical interpretation. J. Atmos. Sci. 74 (4), 1011–1037.
Heavens, N.G., Cantor, B.A., Hayne, P.O., Kass, D.M., Kleinböhl, A., McCleese, D.J., Piqueux, S., Schofield, J.T., Shirley, J.H., 2015. Extreme detached dust layers near Martian volcanoes: evidence for dust transport by mesoscale circulations forced by high topography. Geophys. Res. Lett. 42 (10), 3730–3738.
Heavens, N.G., Richardson, M.I., Kleinböhl, A., Kass, D.M., McCleese, D.J., Abdou, W., Benson, J.L., Schofield, J.T., Shirley, J.H., Wolkenberg, P.M., 2011. The vertical distribution of dust in the Martian atmosphere during northern spring and summer: observations by the Mars Climate Sounder and analysis of zonal average vertical dust profiles. J. Geophys. Res. 116 (E4), E04003.
Kahre, M.A., Murphy, J.R., Haberle, R.M., 2006. Modeling the Martian dust cycle and surface dust reservoirs with the NASA Ames general circulation model. J. Geophys. Res. 111 (E6), E06008.
Kass, D.M., Kleinböhl, A., McCleese, D.J., Schofield, J.T., Smith, M.D., 2016. Interannual similarity in the Martian atmosphere during the dust storm season. Geophys. Res. Lett. 43, 6111–6118.
Kleinböhl, A., Schofield, J.T., Kass, D.M., Abdou, W.A., Backus, C.R., Sen, B., Shirley, J.H., Lawson, W.G., Richardson, M.I., Taylor, F.W., Teanby, N.A., McCleese, D.J., 2009. Mars Climate Sounder limb profile retrieval of atmospheric temperature, pressure, and dust and water ice opacity. J. Geophys. Res. 114 (E10), E10006.
Kulowski, L., Wang, H., Toigo, A.D., 2017. The seasonal and spatial distribution of textured dust storms observed by Mars Global Surveyor Mars Orbiter Camera. Adv. Space Res. 59, 715–721.
Liou, K.-N., 1992. Radiation and Cloud Processes in the Atmosphere. Oxford University Press, New York.
Marchand, R., Ackerman, T., Smyth, M., Rossow, W.B., 2010. A review of cloud top height and optical depth histograms from MISR, ISCCP, and MODIS. J. Geophys. Res. 115 (D16), D16206.
Martin, L.J., Zurek, R.W., 1993. An analysis of the history of dust activity on Mars. J. Geophys. Res. 98 (E2), 3221–3246.
Martin, T.Z., Richardson, M.I., 1993. New dust opacity mapping from Viking infrared thermal mapper data. J. Geophys. Res. 98, 10941–10949.
Mischna, M.A., Lee, C., Richardson, M.I., 2012. Development of a fast, accurate radiative transfer model for the Martian atmosphere, past and present. J. Geophys. Res. 117 (E16), E10009.
Montmessin, F., Forget, F., Rannou, P., Cabane, M., Haberle, R.M., 2004. The origin and role of water ice clouds in the Martian water cycle as inferred from a general circulation model. J. Geophys. Res. 109 (E18).
Moore, H.J., 1985. The Martian dust storm of sol 1742. proc. lunar planet. sci. conf. 16. J. Geophys. Res. Suppl. 90, D163–D174.
Murphy, J.R., Pollack, J.B., Haberle, R.M., Leovy, C.B., Toon, O.B., Schaeffer, J., 1995. Three-dimensional numerical simulation of Martian global dust storms. J. Geophys. Res. 100 (E12), 26357–26376.
Newman, C.E., Lewis, S.R., Read, P.L., Forget, F., 2002. Modeling the Martian dust cycle: 2. Multiannual radiatively active dust transport simulations. J. Geophys. Res. 107 (E12). doi:10.1029/2002JE001920.
Newman, C.E., Richardson, M.I., 2015. The impact of surface dust source exhaustion on the Martian dust cycle, dust storms and interannual variability, as simulated by the MarsWRF General Circulation Model. Icarus 257, 47–87.
Rafkin, S.C.R., 2009. A positive radiative-dynamic feedback mechanism for the maintenance and growth of Martian dust storms. J. Geophys. Res. 114 (E1), E01009.
Richardson, M.I., Toigo, A.D., Newman, C.E., 2007. PlanetWRF: a general purpose, local to global numerical model for planetary atmospheric and climate dynamics. J. Geophys. Res. 112. doi:10.1029/2006JE002825.
Ryan, J.A., Henry, R.M., 1979. Mars atmospheric phenomena during major dust storms, as measured at surface. J. Geophys. Res. 84 (B6), 2821–2829.
Schneider, E.K., 1983. Martian great dust storms - interpretive axially symmetric models. Icarus 55 (2), 302–311.
Smith, M.D., 2008. Spacecraft observations of the Martian atmosphere. Ann. Rev. Earth Planet. Sci. 36, 191–219.
Spiga, A., Faure, J., Madeleine, J.-B., Määttänen, A., Forget, F., 2013. Rocket dust storms and detached dust layers in the Martian atmosphere. J. Geophys. Res. 118 (4), 746–767.
Strausberg, M.J., Wang, H., Richardson, M.I., Ewald, S.P., Toigo, A.D., 2005. Observations of the initiation and evolution of the 2001 Mars global dust storm. J. Geophys. Res. 110 (E2). doi:10.1029/2004JE002361.
Toigo, A.D., Lee, C., Newman, C.E., Richardson, M.I., 2012. The impact of resolution on the dynamics of the Martian global atmosphere: varying resolution studies with the MarsWRF GCM. Icarus 221 (1), 276–288.
Toigo, A.D., Richardson, M.I., Wilson, R.J., Wang, H., Ingersoll, A.P., 2002. A first look at dust lifting and dust storms near the south pole of Mars with a mesoscale model. J. Geophys. Res. 107 (E7). doi:10.1029/2001JE001592.
Wang, H., Richardson, M.I., 2015. The origin, evolution, and trajectory of large dust storms on Mars during Mars years 24–30 (1999–2011). Icarus 251, 112–127.
Wang, H., Richardson, M.I., Wilson, R.J., Ingersoll, A.P., Toigo, A.D., Zurek, R.W., 2003. Cyclones, tides, and the origin of a cross-equatorial dust storm on Mars. Geophys. Res. Lett. 30 (9), 1488–1491.
Wilson, R.J., 1997. A general circulation model simulation of the Martian polar warming. Geophys. Res. Lett. 24 (2), 123–126.